The influence of volcanic eruptions on the climate of tropical South America during the last millennium in an isotope-enabled GCM

Christopher M. Colose[1], Allegra N. LeGrande[2], Mathias Vuille[1]

[1] Dept. of Atmospheric & Environmental Sciences, University at Albany, SUNY, Albany, NY 12222

[2] NASA Goddard Institute for Space Studies, New York, NY, 10025

Correspondence to: Christopher Colose (ccolose@albany.edu)

Abstract

Currently, little is known on how volcanic eruptions impact large-scale climate phenomena such as South American paleo-ITCZ position and summer monsoon behavior. In this paper, an analysis of observations and model simulations is employed to assess the influence of large volcanic eruptions on the climate of tropical South America. This problem is first considered for historically recent volcanic episodes for which more comprehensive global observations exist, but also where fewer events and the confounding effects of ENSO lead to inconclusive interpretation of the impact of volcanic eruptions at the continental scale. Therefore, we also examine a greater number of reconstructed volcanic events for the period 850 C.E. to present that are incorporated into the NASA GISS ModelE2-R simulation of the Last Millennium.

An advantage of this model is its ability to explicitly track water isotopologues throughout the hydrologic cycle and simulating the isotopic imprint following a large eruption. This effectively removes a degree of uncertainty associated with error-prone conversion of isotopic signals into climate variables, and allows for a direct comparison between GISS simulations and paleoclimate proxy records.

Our analysis reveals that both precipitation and oxygen isotope variability respond with a distinct seasonal and spatial structure across tropical South America following an eruption. During austral winter, the heavy oxygen isotope in precipitation is enriched, likely due to reduced moisture convergence in the ITCZ domain and reduced rainfall over northern South America. During austral summer, however, precipitation is depleted in heavy isotopes over Amazonia, despite reductions in rainfall, suggesting that the isotopic

response is not a simple function of the 'amount effect.' During the South American monsoon season, the amplitude of the temperature response to volcanic forcing is larger than the rather weak and spatially less coherent precipitation signal, complicating the isotopic response to changes in the hydrologic cycle.

1. Introduction

70

71 1.1. Volcanic Forcing on Climate

72

73 Plinian (large, explosive) volcanic eruptions are a dominant driver of naturally
74 forced climate variability during the Last Millennium (LM, taken here to be 850 C.E. to
75 present; e.g., Stothers and Rampino, 1983; Hansen et al., 1992; Crowley et al., 2000;
76 Robock et al., 2000; Robock, 2003; Goosse et al., 2005; Yoshimori et al., 2005; Emile-
77 Geay et al., 2008; Cole-Dai, 2010; Timmreck, 2012; Iles et al., 2013; Schurer et al.,
78 2014). In addition to their importance for 20th century climate, they are the largest
79 magnitude external forcing during last 1000 years of the pre-industrial period, the most
80 recent key interval identified by the Paleoclimate Modelling Intercomparison Project
81 Phase III (PMIP3). As such, these eruptions serve as a natural testbed to assess the skill
82 of climate models in simulating how climate responds to external perturbations.
83 Although the most significant climate impacts of eruptions are realized over just a
84 few years following the eruption, they provide the source of the largest amplitude
85 perturbations to Earth's energy budget during the LM. For example, the eruption of Mt.
86 Pinatubo in June 1991, although transitory, exerted a radiative forcing comparable to an
87 instantaneous halving of atmospheric CO_2 [Hansen et al., 1992; Minnis et al., 1993; see
88 also Driscoll et al. (2012) for models in the Coupled Model Intercomparison Project
89 Phase 5 (CMIP5)]; several paleo-eruptions during the LM likely had an even larger
90 global impact (Figure 1).
91 The principle climate impact from volcanic eruptions results from the liberation
92 of sub-surface sulfur-containing gases such as sulfur dioxide, which are injected into the

93 stratosphere and react with water to form sulfate aerosols (e.g., Harshvardhan and Cess,
94 1976; Coakley and Grams, 1976; Pollack et al., 1976, 1981; Lacis et al., 1992). The most
95 pronounced impact of large tropical eruptions includes a radiatively cooled troposphere
96 and heated stratosphere (e.g., Lacis et al., 1992; Robock and Mao, 1995; Stenchikov et al.,
97 1998). Sulfate aerosols from the Mt. Pinatubo eruption grew from a background effective
98 radius of ~0.2 μm up to ~0.8 μm, strongly scattering incoming solar radiation. For sulfate
99 aerosols in this size range, this shortwave scattering is 5-10x larger than the increase in
100 infrared opacity from the aerosols, and results in a warming stratosphere and cooling of
101 Earth's surface (Turco et al., 1982; Lacis et al., 1992).
102 Studies on the impacts of volcanic eruptions have generally focused on global or
103 Northern Hemisphere metrics (e.g., Lucht et al., 2002; Gillett et al., 2004; Shindell et al.,
104 2004; Oman et al., 2005; Oman et al., 2006; Anchukaitis et al., 2010; Peng et al., 2010;
105 Evan et al., 2012; Zhang et al., 2013; Man et al., 2014), for instance in examining
106 responses to the East Asian monsoon system (EAMS) or the Arctic Oscillation.
107 Comparatively little attention has been given to the Southern Hemisphere, or to South
108 America specifically (although see Joseph and Zeng, 2011, and Wilmes et al., 2012).
109 Some previous work has focused on the Southern Annular Mode in the ERA-40 and
110 NCEP/NCAR reanalysis, in addition to a previous version of NASA Goddard Institute
111 for Space Studies (GISS) Model-E (Robock et al., 2007) and in a subset of CMIP3
112 models (Karpechko et al., 2010) or in CMIP5 (Gillett and Fyfe, 2013).
113 How volcanic forcing is expressed over South America remains an important
114 target question for several reasons. First, recognition of the South American monsoon
115 system (SAMS) as an actual monsoon system is less than two decades old (Zhou and Lau,

116 1998), and thus study of SAMS dynamics is still relatively young (section 1.3) and very
117 little work has been done specifically focused on volcanic eruptions. For instance, should
118 we expect to see a reduction in austral summer rainfall (during the monsoon season) as
119 has been reported for the EAMS (Man et al., 2014)? Secondly, the largest volcanic
120 eruptions during the late 20th century (e.g., Mt. Agung, 1963, Indonesia; El Chichón,
121 1982, Mexico; Mt. Pinatubo, 1991, Island of Luzon in the Philippines- hereafter, these
122 three events are referred to as L20 eruptions) occur quasi-simultaneously with an
123 anomalous El Niño-Southern Oscillation (ENSO) state, and in general represent a small
124 sample size in a noisy system. This limits the prospect of robust hypothesis testing and
125 guidance for what impacts ought to be expected following large eruptions at the
126 continental scale. Finally, South America offers promise for a comparatively dense
127 network of high-resolution proxy locations relative to other tropical regions (see below),
128 offering the potential to detect whether South American hydroclimate signals to large
129 eruptions are borne out paleoclimatically.
130 In this study, we explore the post-volcanic response of South American climate
131 operating through the vehicle of unique model simulations (spanning the LM) using the
132 recently developed GISS ModelE2-R (LeGrande et al., 2015, in prep; Schmidt et al.,
133 2014a), which allows for the sampling of a greater number of events than is possible over
134 the instrumental period. Emphasis is placed on temperature and precipitation, but a novel
135 part of this study extends to the response of water isotopologues (e.g., $H_2{}^{18}O$)
136 [colloquially referred to hereafter as 'isotopes' and expressed as $\delta^{18}O$ in units per mil (‰)
137 vs. Vienna Standard Mean Ocean Water]. The isotopic composition of precipitation

138 ($\delta^{18}O_p$) is a key variable that is directly derived from proxy data used in tropical
139 paleoclimate reconstructions.
140 The aim of this paper is to create a potentially falsifiable prediction for the
141 isotopic imprint that a volcanic eruption should tend to produce across the South
142 American continent. The ability to explicitly model the isotopic response allows for a less
143 ambiguous comparison of simulations and paleoclimate records and for hypothesis
144 testing. It is unclear whether or not the current proxy archives are suitable to test such a
145 prediction with high confidence, given dating uncertainties (in both proxies and in the
146 actual timing of eruptions), or the level of noise in proxy data and the real world.
147 Additionally, the prevailing high-resolution archives in South America only feature a few
148 tropical records (Vimeux et al., 2009; Neukom and Gergis, 2012; Vuille et al., 2012).
149 Nonetheless, the growing number of high-resolution records offers hope that testing the
150 modeled response to high-frequency volcanic signals will be an avenue for future
151 research. This can also better inform debate centered on the inverse problem in
152 interpreting isotopic signals (i.e., what do observed changes in proxy data imply about
153 past climate changes?), which remains contentious (section 1.4).
154 The structure of this article is as follows: in the remaining part of section 1, we
155 summarize previous literature on the impact of large volcanic eruptions on paleoclimate,
156 in addition to a discussion of South American climate. Section 2 presents data and
157 methodology, including how volcanic forcing is implemented in ModelE2-R. Section 3
158 discusses our results and we end with conclusions in section 4.
159
160 1.2. Volcanic forcing during the Last Millennium

Volcanic forcing has had a very large influence on the climate of the LM (Crowley, 2000; Hegerl et al., 2003; Shindell et al., 2004; Mann et al., 2005; Hegerl et al., 2006; Fischer et al., 2007; D'Arrigo et al., 2009; Timmreck, 2012; Esper et al., 2013; Ludlow et al., 2013; Schurer et al., 2014). Several studies (Miller et al., 2012; Schurer et al., 2014; Atwood et al., 2016; McGregor et al., 2015) collectively provide a compelling case that volcanic forcing may be substantially more important than solar forcing on a hemispheric-to-global scale during the LM, in addition to driving a large portion of the inter-annual to multi-decadal variability in LM simulations (Schmidt et al., 2014b).

Two volcanic forcing datasets (Gao et al., 2008; Crowley and Unterman, 2013) relying on ice core reconstructions of volcanism are used as input in the LM ModelE2-R simulations (and are the CMIP5/PMIP3 LM standard), as discussed in Section 2.

1.3. Tropical South American Climate

South America is home to nearly 390 million people. The continent spans a vast meridional extent (from ~10 °N to 55 °S), contains the world's largest rainforest (the Amazon), in addition to one of the driest locations on Earth (the Atacama desert). The continent has diverse orography, spanning the high Andes along the Pacific to Laguna del Carbón in Argentina, the lowest point in the Southern Hemisphere. Because of this, South America hosts a rich diversity of climate zones and biodiversity, all of which may respond in unique ways to external forcing.

The most prominent climatic feature of tropical and subtropical South America is

184 the South American monsoon system (Zhou and Lau, 1998; Marengo et al., 2001; Vera et
185 al., 2006; Garreaud et al., 2009; Marengo et al., 2012). Much of South America is in a
186 monsoon regime, with tropical/subtropical rainfall over the continent exhibiting a
187 pronounced seasonal cycle. Unlike other monsoon systems such as that in Asia, low-level
188 easterly winds prevail during the entire year in tropical South America, although the wind
189 anomalies do change direction when the annual mean wind field is removed from winter
190 and summer composites (Zhou and Lau, 1998).

191 During austral winter, the maximum in continental precipitation is largely
192 restricted to north of the equator, in a band-like pattern associated with the oceanic Inter-
193 Tropical Convergence Zone (ITCZ). During austral summer, convection is displaced
194 from northwestern South America, and a band of heavy precipitation covers much of the
195 continent, from the southern Amazon Basin to central Brazil and northern Argentina. A
196 distinctive feature of the SAMS is the South Atlantic Convergence Zone (SACZ), a band
197 of cloudiness and precipitation sourced primarily from the tropical Atlantic that extends
198 diagonally (southeastward) from the Amazon towards southeastern Brazil (Figure 2).

199 The SAMS onset occurs around the end of October and the demise between the
200 end of March and April (e.g., Nogués-Paegle et al., 2002; Vera et al., 2006; Silva and
201 Carvalho, 2007). The dominant mode of intraseasonal precipitation variability over South
202 America during summer exhibits a dipole pattern (Nogués-Paegle and Mo, 1997),
203 seesawing between the SACZ region and Southeastern South America, the latter
204 including the densely populated La Plata basin with local economies strongly dependent
205 on agricultural activities.

206 The SAMS is strongly modulated by ENSO behavior on inter-annual timescales
207 (Vuille and Werner, 2005; Garreaud et al., 2009). In general, SAMS-affected regions of
208 tropical South America tend to experience drier than normal conditions during El Niño,
209 while conditions in subtropical latitudes are anomalously humid, including the
210 southeastern part of the continent. Surface air temperatures tend to be anomalously warm
211 in tropical and subtropical South America during El Niño events. These relationships
212 depend somewhat on the time of year, and during La Niña events, the pattern is
213 essentially reversed.
214
215 1.4. Recent South American Monsoon reconstructions from isotopic proxies
216
217 SAMS variability spanning most of the Holocene has been diagnosed from
218 speleothem records in the Peruvian Andes (Kanner et al., 2013) and a review focused on
219 the last 1,000-2,000 years was given in Bird et al. (2011) and Vuille et al. (2012). In all
220 cases, a critical piece of information that is required to properly diagnose paleo-SAMS
221 variability is the ability to translate oxygen isotope variability from natural recorders into
222 a physical climate signal of interest.
223 Early work on isotopes in ice core records from the tropical Andes detected a
224 Little Ice Age (LIA) signal in the oxygen isotope composition of the ice, with results
225 initially interpreted to reflect variations in local temperature due to their resemblance to
226 ice core records from Greenland (e.g., Thompson et al., 1995, 1998) and due to their
227 isotopic enrichment over the past 150 years, in parallel with rising global mean
228 temperatures (Thompson et al., 2006). A temperature-dependence to oxygen isotope

variability has been long known and is particularly important in mid-to-high latitudes (Dansgaard, 1964) and is most directly related to the ratio of initial and final water vapor content of a parcel that is transported horizontally, rather than the temperature-dependence of fractionation itself (Hoffman and Heimann, 1997).

This interpretation in the tropics has been challenged through a number of observational and modeling efforts (Hardy et al., 2003; Vuille and Werner 2005; Vimeux et al., 2005, 2009; Kanner et al., 2012) which suggest that the isotopic signal is more closely related to the degree of rainout upstream in regions of intense convection (in the case of South America, over the Amazon basin). Additionally, since sea surface temperatures (SST) in the Pacific have a large influence on SAMS intensity on inter-annual timescales in the present, oxygen isotope variability over much of tropical South America is linked to the state of the equatorial Pacific (Bradley et al., 2003; Vuille et al., 2003a,b).

In regimes that are highly convective in nature as in tropical South America, empirical evidence shows that the amount of precipitation (the so-called "amount effect", Dansgaard, 1964) rather than the condensation temperature correlates most strongly with $\delta^{18}O_p$ variability, at least on seasonal to inter-annual time scales. In reality, however, the rainout most relevant for the oxygen isotope signal may be at a significant distance from the site where the proxy is derived, potentially complicating the use of local calibrations to climatology as a guide for $\delta^{18}O_p$ interpretations (Schmidt et al., 2007). Isotopic concentrations are explainable as being a function of original concentration, rainout along the moisture transport path, and mixing.

The influence of precipitation amount on $\delta^{18}O_p$, in addition to changes in the

252 partitioning of precipitation sources, has also been identified on decadal to orbital
253 timescales through speleothem records and lake sediments (Cruz et al., 2005; Van
254 Breukelen et al., 2008; Bird et al., 2011; Kanner et al., 2012). These studies have also
255 highlighted the role of latitudinal displacements of the ITCZ, which is ultimately the
256 main moisture conduit for precipitation over the South American continent. Furthermore,
257 many records collected throughout South America now provide evidence for enriched
258 $\delta^{18}O_p$ values during the Medieval Climate Anomaly, which is indicative of weakened
259 SAMS convection and rainout, followed by depleted $\delta^{18}O_p$ values, suggesting heavier
260 rainfall during the LIA in tropical South America (Bird et al., 2011; Apaestegui et al.,
261 2014) with an opposite response in Northeast Brazil (Novello et al., 2012). This, in turn,
262 has been interpreted in terms of North Atlantic SST anomalies (Vuille et al., 2012; Ledru
263 et al., 2013) and the position of the Atlantic ITCZ.

264 Nonetheless, oxygen isotopes respond in unique ways depending on the climate
265 forcing of interest. Indeed, a unique, quantitative local relationship between an isotope
266 record and any particular climate variable of interest is unlikely to hold for all timescales
267 and prospective forcing agents (Schmidt et al., 2007) thus motivating the use of forward
268 modeling to work in conjunction with proxy-based field data. For the remainder of this
269 paper, we focus specifically on the volcanic forcing response.

270

271 **2. Methodology**

272

273 2.1. Data

274

The primary tool used in this study is the water isotope-enabled GISS ModelE2-R. ModelE2-R is a fully coupled atmosphere-ocean GCM (LeGrande et al., 2015, in prep; Schmidt et al., 2014a) that explicitly tracks stable water isotopes. The version used here is the same as the non-interactive atmospheric composition (NINT) physics version used in the CMIP5 experiments (Miller et al., 2014). The current model features 2° latitude x 2.5° longitude horizontal resolution and 40 vertical levels in the atmosphere up to 0.1 hPa, and is coupled to the Russell Ocean that conserves heat, water mass, and salt (Russell et al., 1995) at 1° x 1.25° resolution with 32 vertical levels. ModelE2-R includes stratospheric dynamics and prescribed ozone and aerosol species.

Due to uncertainties in past radiative forcing, a suite of LM simulations using ModelE2-R have been run with different combinations of plausible solar, volcanic, and anthropogenic land use histories (Schmidt et al., 2011, 2012) but with identical greenhouse gas and orbital evolution. These simulations span the period 850-2005 C.E. There are two reconstructions of past volcanic activity (Gao et al., 2008; Crowley and Unterman, 2013) that are used in six combinations of the ModelE2-R LM simulations (see the 'past1000' experimental design at http://data.giss.nasa.gov/modelE/ar5/, and below).

For the LM, three forcing combinations are available in the GISS ModelE2-R simulations that use the Crowley reconstruction for volcanic perturbations. These include Pongratz et al. (2008) [land]/ Krivova et al. (2007) [solar], Kaplan et al (2010) [land]/Krivova et al. (2007) [solar], and Pongratz et al. (2008) [land]/Steinhilber et al. (2009) [solar] (see Schmidt et al., 2011, 2012). We focus only on results from the Crowley reconstruction prior to 1850 CE due to a mis-scaling of the Gao forcing in the

298 model that roughly doubled the appropriate radiative forcing. For the historical period
299 (1850-present), the volcanic forcing history is based on Sato et al. (1993) and is
300 equivalent among the different (six) simulation members.

301 Water isotope tracers are incorporated into the model's atmosphere, land surface,
302 sea ice, and ocean. These isotopes are advected and tracked through every stage of the
303 hydrologic cycle. At each phase change (including precipitation, evaporation, ice
304 formation or melting) an appropriate fractionation factor is applied (Schmidt et al., 2005)
305 and all freshwater fluxes are tagged isotopically. Stable isotope results from the lineage
306 of GISS models have a long history of being tested against observations and proxy
307 records (e.g., Schmidt et al., 2007; LeGrande and Schmidt, 2008, 2009; Lewis et al., 2010,
308 2013, 2014; Field et al., 2014).

309 Crowley and Unterman (2013) discuss the details behind the LM Aerosol Optical
310 Depth (AOD) reconstruction that defines the volcanic forcing time-series in ModelE2-R
311 (Figure 1). This estimate is derived from sulfate peaks in ice cores, which are relatively
312 well dated and referenced to the historical record during the satellite era. Crowley and
313 Unterman (2013) provide an AOD history over 4 latitude bands (from 0-30° and 30-90°
314 in both hemispheres). ModelE2-R uses a cubic spline to interpolate this forcing dataset
315 over 24 latitude bands. The choice of volcanic eruptions used for the LM analysis
316 (section 2.2 below) is based on the AOD dataset from this 24-latitude grid.

317 In addition to the model, we briefly explore post-L20 eruption results in the
318 instrumental record. To do this, we take advantage of the NASA GISS Surface
319 Temperature analysis (GISTEMP) land-ocean index (Hansen et al., 1999), and Global
320 Precipitation Climatology Centre (GPCC) v6, a monthly precipitation dataset over land

321 (Schneider et al., 2011). For Figures 2 and 3 where ocean climatological data is shown,
322 we use the Global Precipitation Climatology Project (GPCP) version 2.2 (Adler et al.,
323 2003), a combined land station and satellite product available since 1979. These datasets
324 are called upon to gauge the tropical climate response following the three L20 eruptions.
325 We use the 2.5° resolution GPCC dataset, as that is comparable to the GISS model and
326 what is justified by the station coverage in this part of the world. The GPCC product
327 offers considerably better global and South American coverage than other precipitation
328 datasets, although observational density for rainfall is still considerably more problematic
329 over South America than for many other regions of the globe. There is a sharp drop-off in
330 the number of rain gauge stations used earlier in the 20th century over much of the South
331 American continent. Figure S1 shows the station density at the time of each L20 eruption,
332 as well as the total number of land stations over South America with time.
333 Finally, in section 3.1 we present data from the Global Network of Isotopes in
334 Precipitation (GNIP) accessible from the International Atomic Energy Agency (IAEA)
335 for $\delta^{18}O_p$, as a test of the model's ability to track the seasonal hydrologic cycle in the
336 form of its isotopic response over South America before discussing the Last Millennium
337 results. Unfortunately, there is considerable spatial and temporal heterogeneity in the
338 GNIP data over South America. In fact, only a few stations have data overlap with one or
339 two eruptions and with a sufficient number of $\delta^{18}O_p$ data points to establish reasonable
340 seasonal or annual statistics. Additionally, the post-volcanic (L20) anomalous isotope
341 field over South America strongly resembles the ENSO expression on the isotope field
342 (Vuille et al., 2003a) and with large spread between events (not shown). This suggests
343 that internal variability (ENSO) dominates the forced (volcanic) response in this very

small historical sample size, thereby leaving little hope that the prevailing network of observations is suitable for hypothesis testing and model validation in our context.

2.2 Super-posed Epoch and Composite Analysis

We present the spatial pattern of observed and simulated response for temperature and precipitation over land for two L20 eruptions (El Chichón and Mt. Pinatubo). Results are shown for annual-means in 1983 and 1992. We choose only two for brevity, as our argument that assessing the signal in any specific region is difficult in a small sample of eruptions is unaffected. Because of the dominant influence of unforced variability on tropical South American climate (Garreaud et al., 2009) overriding the volcanic signal during the L20 eruptions, we instead present a superposed epoch anomaly composite of the tropical-mean temperature anomaly, zonally averaged from 30°S to 30°N. Results are shown for years -3 to +5, with zero defining the time of the eruption. This composite is formed for all three L20 eruptions. In all cases, the five years prior to the eruption were subtracted from the superposed composite. Other sensible choices for the non-eruption reference period do not significantly change the results.

For the full LM spatial composites, we use only eruptions where vertically integrated (15 to 35 km) stratospheric AOD averaged from 30°N to 30°S exceeds 0.1 for at least 12 consecutive months in the simulation (top panel in Figure 1). For the LM composites, we focus only on seasonal (DJF and JJA) composites, and a given season will enter the composite if at least 2/3 months meet the AOD threshold; this criterion yields 15 eruptions since 850 C.E. The selection of events used in the LM composite is

367 very weakly sensitive to this choice of latitude band. Mt. Pinatubo is the only L20
368 eruption in this composite, and is actually one of the smallest eruptions in this selection
369 based on the maximum AOD encountered near the time of the eruption (see Table 1 for
370 dates of each event). We believe sampling a larger number of events with greater forcing
371 is a better way to understand the volcanic response in this model, rather than increasing
372 the ensemble size for the L20 events. We do stress, however, that there is considerable
373 forcing uncertainty during the LM and so the model results ought to be viewed as a slave
374 to the imposed AOD and particle size distribution.

375 For the LM "non-eruption" fields, we use 15 years prior to the eruption as a
376 reference period to calculate the anomaly for each event, unless another event occurs
377 during that time (overlap occurs only once for eruptions in 1809 and 1815) in which case
378 the pre-1809 climatology is used twice. The exception is for Mt. Pinatubo, which again
379 uses the previous five years to calculate the anomaly. When constructing seasonal
380 averages of $\delta^{18}O_p$, the oxygen isotope value for each month is weighted by the
381 precipitation amount during that month, at each grid cell.

382 Since each post-eruption difference field is computed using the immediate
383 response minus a local 15-year climatology, time is not relevant in this analysis and so
384 we use all three members with the Crowley forcing (representing over 3,000 years of
385 simulation time) to generate a composite that features 45 volcanic "events" (15 eruptions
386 in each of the three members). In the historical (post-1850) extension of these runs, the
387 coding error that resulted in a mis-implementation of the Gao forcing is not an issue, and
388 so we use six ensemble members each (three volcanic events in six ensemble members)
389 for the L20 results.

390 The ensemble-mean composite results displayed for the LM eruptions include
391 contributions from three members that differ not just in the internal variability, but also in
392 their solar and land-use forcing. Similarly, the L20 results are from model runs that also
393 include other transient historical forcings occurring at the time of the eruption, including
394 greenhouse gas increases throughout the duration of the event (although these forcings
395 are the same among all ensemble members). However, in all cases we focus only on the
396 immediate years after the eruption. Since the primary signal of interests is expected to be
397 large compared to the impact of more slowly varying and smaller-amplitude forcings, the
398 ensemble spread for a given eruption can be interpreted as a sampling of the model
399 internal variability coincident with the event. We have tested our composite results using
400 the same dates as our volcanic events in simulations with other varying forcings but with
401 no volcanoes (there are no volcano-only runs with this model version for the LM), and
402 the results are indistinguishable from noise (not shown). The LM composite results are
403 discussed in section 3.2.
404 Finally, it is now well appreciated that any climate response under investigation
405 will be shackled to the spatial structure of the forcing imposed on a model. For example,
406 preferential heating/cooling of one hemisphere will induce different tropical precipitation
407 responses than a well-mixed gas that behaves CO_2-like (Kang et al., 2008, 2009; Frierson
408 and Hwang, 2012; Haywood et al., 2012). Figures S2 and S3 show the latitudinal AOD
409 distribution structure for all eruptions used in the generation of the LM composites within
410 ModelE2-R. The mean of all events is rather symmetric between hemispheres (though
411 somewhat skewed toward the Southern Hemisphere tropics), and similar to the pattern
412 expected with CO_2 change, the forcing is largest in the tropics. Thus, the resulting climate

413 responses outlined in this paper ought to be viewed as a response consistent with a
414 forcing that is relatively symmetric about the equator. Results from volcanic eruptions
415 with emphasis on the spatial structure of forcing will be reported in a separate paper.
416
417 2.3. Influence of ENSO on the Late 20th Century (L20) eruptions
418
419 For the L20 volcanic events, El Niño events are occurring quasi-simultaneously
420 with the eruption. This introduces a pervasive issue when attempting to isolate the
421 volcanic signal (e.g., Robock, 2003; Trenberth and Dai, 2007; Joseph and Zeng, 2011)
422 and is particularly important over South America (e.g. Garreaud et al., 2009).
423 In order to remove the effects of ENSO from the super-posed epoch and spatial
424 composite analyses described above in the GISTEMP and GPCC data, we first perform a
425 multiple regression with the variable of interest over the period 1951-2005 using a linear
426 time trend and the Niño 3 index as predictors (5°N-5°S, 150°W -90°W, data from
427 http://www.cpc.ncep.noaa.gov/data/indices/) over the same period, excluding two years
428 of data after each L20 eruption. At each grid cell, the Niño 3 index is lagged from 0-6
429 months and the correlation coefficient with the maximum absolute value (since a positive
430 index can induce a negative anomaly in the variable of interest) is found. This is similar
431 to the approach used in Joseph and Zeng (2011), allowing the maximum ENSO influence
432 to be removed at each grid point at the expense of contemporaneous relationships. The
433 lagged Niño index is then regressed against the time series of each variable and the
434 residual from this regression is retained. This approach assumes a linear relationship
435 between ENSO and the climate response over South America, an assumption that appears

436 justified on inter-annual to decadal time scales (Garreaud et al., 2009).

437 For each of the six ensemble members used in the model L20 composite, a similar
438 procedure is performed in which the Niño 3 index (consistent with the realization of the
439 Niño 3 domain SSTs in that model simulation) is calculated and regressed out in the same
440 manner. For the full LM computations, the number of larger-amplitude events in the
441 three-ensemble member composite should help average out the influence of Pacific SST
442 variability, and no ENSO removal procedure is applied.

443

444 **3. Results and Discussion**

445

446 3.1. L20

447

448 Figure 3 illustrates that ModelE2-R reproduces the seasonal cycle of
449 climatological rainfall (comparing Figure 3a with 3b) and oxygen isotope distribution
450 (comparing Figure 3c with 3d) with some fidelity over South America. This includes a
451 meridional migration of the ITCZ toward the summer hemisphere and an intensification
452 of the South American monsoon during DJF. Where data permit (Figure 3c) there is good
453 agreement between model and observations, both displaying oxygen isotope DJF
454 enrichment relative to JJA in the tropics north of the equator and the higher latitudes
455 south of 30°S, and depletion in the continental interior south of the equator associated
456 with the monsoon wet season. ModelE2-R (Figure 3b) tends to produce too much
457 precipitation over northeastern Brazil although the gross features of the seasonal
458 migration in rainfall are well captured. This ability to accurately simulate the seasonality

459 of $\delta^{18}O_p$ over the tropical Americas has also been noted in two atmospheric GCMs with
460 no coupled ocean (NASA-GISS II and ECHAM-4, see Vuille et al., 2003a).
461 Figure 4 shows the ENSO-removed super-posed epoch analysis for tropical
462 temperature associated with the recent three L20 eruptions. There is good agreement
463 between the observed and modeled temperature response, both in amplitude and recovery
464 timescale. The tropical-mean cooling is on the order of several tenths of a degree, and
465 larger after Mt. Pinatubo (not shown individually).
466 The spatial structure of the post- El Chichón and Pinatubo events in land
467 observations and the individual model realizations are shown in Figures 5 and 6,
468 respectively. Observations exhibit cooling over much of the globe, especially after Mt.
469 Pinatubo that is largely reproduced by the model. However, there is considerable spread
470 among the individual ensemble members and between the two events, indicating a large
471 role for internal variability in dictating the observed spatial pattern following these events.
472 This is also true over South America.
473 In GISTEMP, the high-latitudes of South America cool more than the tropical
474 region of the continent after Mt. Pinatubo. There is still a residual signal from ENSO in
475 tropical South America following both L20 eruptions that is not reproduced by the model.
476 This is not unexpected, since ENSO events comparable to the magnitude of the historic
477 realizations due not occur coincident with the volcanic forcing in the individual ensemble
478 members. The magnitude of this signal is sensitive to the Niño index used in the
479 regression method described above. Without ENSO removal, tropical South America
480 warms following the two eruptions (not shown). The influence of ENSO appears minimal
481 over the higher latitude sectors of the continent.

The precipitation pattern following the L20 eruptions exhibits substantial variability in space and across eruptions, with a general drying pattern over land in tropical latitudes. South America experiences less precipitation near the equator after Mt. Pinatubo (see also Trenberth and Dai, 2007), a pattern reproduced in some of the ensemble realizations.

It should be noted that model-observation comparison is hindered not just by internal variability, but also by the specified historical volcanic forcing in the model. In fact, the Stratospheric Aerosol and Gas Experiment (or SAGE) II satellite sensor was saturated by the aerosol cloud after Mt. Pinatubo; subsequent work (Santer et al., 2014; Schmidt et al., 2014c) suggests that the forcing following Pinatubo is too large in the CMIP5 generation of models. It is likely that CMIP6/PMIP4 will feature a reduced AOD and different particle size.

Because of the considerable variability seen in observations (following historical eruptions) and also across ensemble members, it is evident that a larger signal-to-noise ratio than is available from the L20 eruptions alone is required to help isolate any volcanic signal. ModelE2-R is the laboratory from which we proceed to sample a larger number of events, some of which contain larger amplitude than the L20 eruptions.

3.2. Last Millennium Composites

3.2.1. Temperature and Precipitation

Figure 7 shows the LM post-volcanic temperature composite for all 45 events. During both seasons, cooling is statistically significant over virtually the entire continent (stippling indicates significance at the 90% level, t-test). The temperature response is strongest in the interior of the continent, particularly during the austral winter. The enhanced high-latitude cooling exhibited in the observations after Mt. Pinatubo does not emerge in the model composite.

The precipitation anomalies for the LM composite are shown in Figure 8. As expected, there is a distinct seasonal structure in the response, with the largest anomaly concentrated in a narrow region north of the equator during austral winter, coincident with the location of climatological rainfall maxima in the region. During JJA, precipitation increases in the North Atlantic region following volcanic eruptions, while very strong and statistically significant precipitation reductions occur just north of the equator (including over northern Brazil, Ecuador, Venezuela, Colombia, and Guyana) and encompassing the northern Amazon Basin. This signal is consistent with a weakening of the moisture flux owing to the decrease in saturation vapor pressure due to cooling that is demanded by Clausius-Clapeyron (Held and Soden, 2006). During this season, the precipitation response is significant virtually everywhere in northern South America. Supplementary Figure (S5) further illustrates that the JJA precipitation response is remarkably robust to all eruptions that enter into the composite.

Figure 9b illustrates the relationship between area-averaged precipitation from 20°S to 0°, 77.5°W to 45°W (for DJF) and 0° to 10°N, 77.5°W to 52.5°W (for JJA) and the maximum AOD encountered for each eruption. These two regions were selected to reflect the seasonal migration of rainfall (Figure 2, 3). 15 eruptions are displayed with the

three-member ensemble spread given for each. Precipitation only increases north of the equator during austral winter in a few model realizations. Moreover, the magnitude of the precipitation response during JJA scales with the size of the eruption, particularly for very large eruptions (e.g., comparing five eruptions with AOD > 0.3 vs. those with smaller perturbations, although the spread amongst the ensemble members is large). The spatial composite for each individual eruption (each averaged over the three ensemble members) is shown in Figure S5.

The precipitation response during austral summer is more difficult to interpret (Figure 8a). During this season, the zonally oriented Atlantic ITCZ migrates southward and the SACZ becomes more intense as it is connected with the area of convection over the central and southeastern part of the continent. It is noteworthy that the land cools substantially more than the surrounding ocean (Figure 7), which one could expect to weaken the monsoon-sourced precipitation during DJF. While precipitation is indeed reduced over the tropical continent, the response is weaker than in JJA and less spatially coherent, with many areas failing to meet statistical significance. An analysis of the individual responses reveals that the signal is more eruption-dependent during DJF than during JJA (see Figure S4), with a few events actually exhibiting modest increases in precipitation. Nonetheless, there is a clear tendency for reduced DJF precipitation within the SAMS region, although there is little to no dependence of the mean rainfall anomaly on the magnitude of the AOD perturbation, at least above the 0.1 threshold used in this study (Figure 9b), unlike for equatorial South America during JJA. Conversely, the temperature response (Figure 9a) depends on the size of the eruption in both seasons, as is expected.

3.2.2. Tropical Hydroclimate Response

Since the South American climate is intimately linked to large-scale tropical dynamics, the global precipitation composite is shown in Figure S6 to better inform the model response. The most robust signal is characterized by a reduction in tropically averaged precipitation and the tendency for wet regions to become drier, and dry regions to become wetter (see also Iles et al., 2013; Iles and Hegerl, 2014), in contrast to the anticipated hydrologic response in a future, higher-CO_2 world (Held and Soden, 2006).

This pattern is a thermodynamic effect linked to reduced moisture convergence within the convergence zones and to reduced moisture divergence in the descending zones of the Hadley cell, which reduces the contrast in values of precipitation minus evaporation (P-E) between moisture convergence and divergence regions (Chou et al., 2009). The complete hydrologic response of the ΔP-E field (not shown) has the same spatial structure as the ΔP field, since evaporation is decreasing nearly everywhere in the tropics. Because both P and E are decreasing on the equator-ward flank of the ITCZ the ΔP-E signal is rather weak in the deep tropics, while ΔP-E increases more rapidly than ΔP in the subtropics.

The tendency for modest precipitation anomalies over the continent during DJF appears to be part of a pattern that spans a broad swath of longitudes across the entire deep tropics in association with the seasonal cycle. Nonetheless, the response during DJF is weaker over land.

573 3.2.3. Oxygen Isotope Anomalies

574

575 In order to relate the responses discussed in the previous sections back to a
576 potentially observable paleoclimate metric, we show the composite $\Delta\delta^{18}O_p$ field for the
577 DJF and JJA seasons in South America (Figure 10). It should be cautioned that much of
578 the isotopic variability that can be observed in proxies within the continental interior or
579 high-elevation glacier sites will likely be seasonally biased toward the wet season months
580 (Hardy et al., 2003).

581 During the JJA season, there is a strong enrichment of the $\delta^{18}O_p$ pattern that is
582 zonally extended over equatorial South America. In addition, there is a corresponding
583 $\delta^{18}O_p$ depletion in the adjacent North Atlantic sector. This response is inextricably
584 coincident with the strong change in precipitation in the ITCZ domain that was assessed
585 in Figure 8, and is broadly consistent with a "rainfall amount" control on the isotopic
586 imprint (Dansgaard, 1964). South of approximately 15°S, the sign of the anomaly
587 reverses to a depletion of the heavy isotope.

588 During the austral summer, volcanic eruptions lead to a clear negative excursion
589 in $\delta^{18}O_p$ over virtually the entire SAMS region, including the Amazon basin, tropical
590 Andes, and eastern Brazil. The statistical significance of the resulting isotopic anomaly
591 extends throughout most of the landmass within the tropics and in the North Atlantic.
592 There are small but non-significant exceptions (positive $\delta^{18}O_p$ excursions) such as in
593 eastern Brazil. The negative excursions also include regions outside of the SAMS belt in
594 the subtropics and mid-high latitudes of South America.

595 The austral summer $\delta^{18}O_p$ depletion is the opposite sign from what one would
596 expect if the reduced precipitation were driving the isotopic response. Thus, it may well
597 be that the strong temperature response to volcanic eruptions dominates the continent-
598 wide oxygen isotope depletion during the DJF season and in the extratropics during JJA
599 over the relatively weak precipitation response. Precipitation on the other hand appears to
600 be the primary control knob of $\Delta\delta^{18}O_p$ during JJA within the ITCZ region.
601 The correlation between $\Delta\delta^{18}O_p$ and temperature or precipitation, based on a
602 regression using all 45 volcanic events, is reported in Figure 9, using the same domains
603 for DJF and JJA described in section 3.2.1. In the case of volcanic forcing it appears that
604 the amplitude of the temperature response to volcanic eruptions over tropical South
605 America is larger than the rather weak and spatially incoherent precipitation signal,
606 although both the temperature and precipitation coefficients must be considered to
607 characterize the isotopic variability during this season (Figure S7). This may explain why
608 the DJF isotopic signal related to volcanic eruptions seems to respond to atmospheric
609 cooling, even in the tropics, where isotopic variability is usually more closely associated
610 with changes in the hydrologic cycle. During JJA, the isotopic enrichment is much more
611 closely associated with precipitation reduction north of the equator, whereas the JJA
612 $\Delta\delta^{18}O_p$-temperature relationship is weak and non-significant.
613 Taken together, these results suggest that the primary controls on oxygen isotope
614 variability are forcing and event-dependent, rather than being determined inherently by
615 the latitude of interest (e.g., "precipitation driven" in the tropics and "temperature driven"
616 in the extratropics). This conclusion is compelled by the fact that the precipitation
617 production and distribution in proxy records are the result of an interaction between

618 multiple scales of motion in the atmosphere, the temperature of air in which the
619 condensate was embedded, and exchange processes operating from source to sink of the
620 parcel deposited at a site. Thus, a consistent description of how to interpret oxygen
621 isotopes into a useful climate signal cannot be given without considering all of these
622 processes and the target process of interest.

623 To further complement the spatial analysis, a composite Hovmöller diagram is
624 utilized (Figure 11) in order to illustrate the time-evolution of the temperature,
625 precipitation, and oxygen isotope response. For this plot, the start of each eruption is
626 defined as the closest January to the first month in which AOD reaches 0.1 in order to
627 illustrate the seasonal evolution (rather than compositing by "month from each eruption"
628 as in Figure 3). Therefore, for all 45 events in the composite, the local AOD may reach
629 this threshold within five months (before or after) of the January baseline point (eruptions
630 in June are rounded up to the following January). The Hovmöller composites are plotted
631 for ten years (beginning January three years prior to the eruption). The closest January
632 point to the start of each eruption occurs in the 37th month of the Hovmöller (solid black
633 line in Figure 11a,b,d). Results are zonally averaged from 77.5°W to 45°W.

634 Figure 11a demonstrates a substantial temperature anomaly that peaks south of
635 10°S (compare also to Figure 7). The cooling lasts for several years following the
636 eruption, and decays gradually until most of the signal is lost (~4 years after the eruption
637 in the South American sector), but remains 0.1-0.2°C colder than the pre-eruption
638 climatology. The zonally averaged peak reductions in South American precipitation
639 anomalies occur over the tropical latitudes and last for a comparable period of time as the
640 maximum temperature response. The precipitation anomaly itself migrates synchronously

641 with the seasonal cycle (red line in Figure 11c maps out the latitude of maximum
642 climatological precipitation averaged over all 15 year climatologies of each 45-member
643 event, as a function of time of year). Figure 11b indicates that the largest precipitation
644 response is confined to the equatorial and northern regions during JJA, with weak
645 protrusion into higher tropical latitudes only 1-2 years after the eruption. The JJA isotopic
646 enrichment in northern South America lasts for two seasons in our composite, while there
647 is sustained isotopic depletion during DJF in the SASM region for about three years
648 (Figure 11d)

649 Figure 12 provides additional statistical insight into the magnitude of the
650 excursions described in this section. Here, we sampled 100 random 45-event composites
651 in a control simulation with no external forcing (each "event", two seasons in length, is
652 defined as an anomaly expressed relative to a pre-eruption climatology as done
653 previously). The anomalies were averaged over the same areas as in Figure 9, with
654 different domains for DJF and JJA. Notably, for both seasons and for all three variables
655 examined, the single 45-event post-volcanic composite (purple square) lies outside the
656 distribution of all sampled 45-event composites constructed with no external forcing.
657 Nonetheless, the distribution for a smaller sample of events (black circles denote the data
658 for each (15) eruption, each averaged over the three ensemble members) shows
659 considerable spread.

660 The $\delta^{18}O_p$ anomalies discussed above result from changes in the isotopic content
661 of precipitation, which may be due to changes in precipitation amount or to other changes
662 in the isotopic composition of the water vapor that condensed to form the precipitate. The
663 changes are not determined by changes in the seasonality of the precipitation. To

664 illustrate this (Figure S8), we decomposed the $\Delta\delta^{18}O_p$ field (see Liu and Battisti, 2015) by
665 weighting the monthly oxygen isotope field by the pre-eruption precipitation values. The
666 results are indistinguishable from the total $\Delta\delta^{18}O_p$ field, suggesting that any changes in
667 monsoon seasonality are negligible in contributing to the isotopic signal, unlike the
668 orbital case considered in Liu and Battisti (2015).
669
670 **4. Conclusions**
671
672 In this study, we have analyzed the response of temperature, precipitation, and
673 $\delta^{18}O_p$ over South America to volcanic forcing associated with large tropical eruptions
674 during the Last Millennium. It is now well known that volcanic eruptions lead to large-
675 scale cooling throughout the tropics, and this result extends to most of the South
676 American continent as well, except in regions that may be simultaneously affected by
677 opposing ENSO behavior. In general, the precipitation response has been more enigmatic,
678 though our results are in broad agreement with numerous other studies showing that there
679 is a substantial decline in tropical-mean precipitation.
680 However, the immediate post-volcanic impact over South America has a complex
681 seasonal and spatial structure. During the austral winter, the precipitation response over
682 the continent is slaved to the response of the large-scale circulation, including a
683 weakening of rainfall intensity within the ITCZ that is migrating northward. In the
684 extratropics, the continent cools and exhibits slight precipitation declines nearly
685 everywhere. Our results suggest the seasonal monsoon precipitation (during DJF) in
686 ModelE2-R exhibits a fairly weak response that is scattered across the continent. It

687 appears that volcanic forcing preconditions the tropical rainfall over the continent to
688 decline during the wet season, but that this response is likely to be eruption-dependent
689 and may be overwhelmed by internal variability.

690 A unique aspect of this study was to probe the $\delta^{18}O_p$ response to volcanic
691 eruptions. During JJA, isotopes become heavily enriched in northern South America as
692 convective activity produces substantially less precipitation. No such relation was found
693 during the monsoon season, even within the tropics, where the large cooling appears to
694 lead to more depleted $\delta^{18}O_p$, despite a weakened hydrologic cycle and reduced monsoon
695 precipitation. In the extratropics, it appears that the temperature decline is driving
696 isotopes toward more depleted values.

697 Unfortunately validation of our model results is hindered by the paucity of
698 observational stable isotope data and by the coincidence of volcanic eruptions with
699 ENSO events over the 20th century. Nonetheless our results may provide some guidance
700 in the search of volcanic signals in high-resolution isotopic proxy data from South
701 America. Given the importance of volcanic forcing for climate variability over the past
702 millennium, and in particular the LIA period, which has been identified as a period of
703 significant climatic perturbation in isotopic proxies from South America, a better
704 understanding of the climatic response to volcanic forcing over this region is urgently
705 needed.

706

707 *Acknowledgments:*

708 This study was funded by NOAA C2D2 NA10OAR4310126 and NSF awards
709 AGS-1003690 and AGS-1303828. We would like to thank NASA GISS for institutional

710 support, in addition to Raphael Neukom and an anonymous reviewer for the constructive
711 comments that helped improve the manuscript. Computing resources supporting this
712 work were provided by the NASA High-End Computing (HEC) Program through the
713 NASA Center for Climate Simulation (NCCS) at Goddard Space Flight Center.
714 GPCP/GPCC data provided by the NOAA/OAR/ESRL PSD, Boulder, Colorado, USA,
715 from their Web site at http://www.esrl.noaa.gov/psd/.
716

References

Adler, R.F., Huffman, G.J., Chang, A., Ferraro, R., Xie, P., Janowiak, J., Rudolf, B., Schneider, U., Curtis, S., Bolvin, D., Gruber, A., Susskind, J., and Arkin, P.: The Version 2 Global Precipitation Climatology Project (GPCP) Monthly Precipitation Analysis (1979-Present), J. Hydrometeor., 4,1147-1167, 2003.

Apaestegui, J., Cruz, F.W., Sifeddine, A., Vuille, M., Espinoza, J.C., Guyot, J.L., Khodri, M., Strikis, N., Santos, R.V., Cheng, H., Edwards, L., Carvahlo E., and Santini, W.: Hydroclimate variability of the northwestern Amazon basin near the Andean foothills of Peru related to the South American Monsoon System during the last 1600 years, Clim. Past, 10, 1967-1981, 2014.

Anchukaitis, K.J., Buckley, B.M., Cook, E.R., Cook, B.I., D'Arrigo, R.D., and Ammann, C.M.: The influence of volcanic eruptions on the climate of the Asian monsoon region, Geophys. Res. Lett., 37, L22703, 2010.

Atwood, A.R., Wu, E., Frierson, D.M.W., Battisti D.S., and Sachs J.P.: Quantifying climate forcings and feedbacks over the last millennium in the CMIP5-PMIP3, J. Climate, 29, 1161-1178, 2016.

Bird, B.W., Abbott, M.B., Rodbell, D.T., and Vuille M.: Holocene tropical South American hydroclimate revealed from a decadally resolved lake sediment $\delta^{18}O$ record, Earth Planet. Sci. Lett., 310, 192-202, 2011.

Bradley, R.S., Vuille, M., Hardy, D.R., and Thompson, L.G.: Low latitude ice cores record Pacific sea surface temperatures, Geophys. Res. Lett., 30, 1174, 2003.

738 Chou, C., Neelin, J.D., Chen, C.A., and Tu, J.Y.: Evaluating the "Rich-Get-Richer"
739 Mechanism in Tropical Precipitation Change under Global Warming, J. Climate, 22,
740 1982–2005, 2009.
741 Coakley, J.A., and Grams, G.W.: Relative Influence of Visible and Infrared Optical
742 Properties of a Stratospheric Aerosol Layer on the Global Climate, J. Appl. Meteor.,
743 15, 679–691, 1976.
744 Cole-Dai, J.: Volcanoes and climate, Wiley Interdisciplinary Reviews: Climate Change,
745 1, 824-839, 2010.
746 Crowley, T.J.: Causes of climate change over the past 1000 years, Science, 289, 270–
747 277, 2000.
748 Crowley, T. J. and Unterman M.B.: Technical details concerning development of a
749 1200-yr proxy index for global volcanism, Earth Syst. Sci. Data, 5, 187–197, 2013.
750 Cruz, F.W., Burns, S.J., Karmann, I., Sharp, W.D., Vuille, M., Cardoso, A.O., Ferrari,
751 J.A., Dias, P.L.S., and Viana, O.: Insolation-driven changes in atmospheric
752 circulation over the past 116,000 years in subtropical Brazil, Nature, 434, 63-66, 2005.
753 Dansgaard, W.: Stable isotopes in precipitation, Tellus, 16, 436–468, 1964.
754 D'Arrigo, R., Wilson, R., and Tudhope, A.: The impact of volcanic forcing on tropical
755 temperatures during the past four centuries, Nature Geosci., 2, 51–56, 2009.
756 da Silva, A. E. and de Carvalho, L. M. V.: Large-scale index for South America Monsoon
757 (LISAM), Atmos. Sci. Lett., 8, 51–57, 2007.
758 Driscoll, S., Bozzo, A., Gray, L.J., Robock, A., and Stenchikov G.: Coupled Model
759 Intercomparison Project 5 (CMIP5) simulations of climate following volcanic
760 eruptions, J. Geophys. Res., 117, D17105, 2012.

761 Emile-Geay, J., Seager R., Cane, M.A., Cook, E.R., and Haug, G.H.: Volcanoes and
762 ENSO over the Past Millennium, J. Climate, 21, 3134–3148, 2008.
763 Esper J., Schneider L., Krusic P.J., Luterbacher J., Büntgen U., Timonen M., Sirocko F.
764 and Zorita E.: European summer temperature response to annually dated volcanic
765 eruptions over the past nine centuries, B. Volcanol. 75, 1-14, 2013.
766 Evan, A.T.: Atlantic hurricane activity following two major volcanic eruptions, J.
767 Geophys. Res., 117, D06101, 2012.
768 Field, R.D., D. Kim, A.N. LeGrande, J. Worden, M. Kelley, and G.A. Schmidt:
769 Evaluating climate model performance in the tropics with retrievals of water isotopic
770 composition from Aura TES, Geophys. Res. Lett., 41, 16, 6030-6036, 2014.
771 Fischer, E.M., Luterbacher, J., Zorita, E., Tett, S.F.B., Casty, C., and Wanner, H.:
772 European climate response to tropical volcanic eruptions over the last half
773 millennium, Geophys. Res. Lett., 34, L05707, 2007.
774 Frierson, D.M.W., and Hwang Y.: Extratropical Influence on ITCZ Shifts in Slab Ocean
775 Simulations of Global Warming, J. Climate, 25, 720–733, 2012.
776 Gao, C., Robock, A., and Ammann, C.: Volcanic forcing of climate over the past 1500
777 years: an improved ice core-based index for climate models, J. Geophys. Res., 113,
778 D23111, 2008.
779 Garreaud, R.D., Vuille, M., Compagnucci, R., and Marengo, J.: Present-day South
780 American climate, Palaeogeogr. Palaeoclimatol. Palaeoecol., 281, 180-195, 2009.
781 Gillett, N.P., Weaver, A.J., Zwiers, F.W., and Wehner, M.F.: Detection of volcanic
782 influence on global precipitation, Geophys. Res. Lett., 31, L12217, 2004.

783 Gillett, N.P., and Fyfe, J.C.: Annular mode changes in the CMIP5 simulations, Geophys.
784 Res. Lett., 40, 1189–1193, 2013.
785 Gonzalez, P.L.M., Polvani, L.M., Seager, R., and Correa, G.J.P.: Stratospheric ozone
786 depletion: a key driver of recent precipitation trends in South Eastern South America,
787 Climate Dyn., 42, 1-18, 2013.
788 Goosse, H., Crowley, T., Zorita, E., Ammann, C., Renssen, H., and Driesschaert, E.:
789 Modelling the climate of the last millennium: what causes the differences between
790 simulations? Geophys. Res. Lett., 32, L06710, doi:10.1029/2005GL22368, 2005.
791 Hansen, J., Lacis A., Ruedy, R., and Sato, M.: Potential climate impact of Mount
792 Pinatubo eruption, Geophys. Res. Lett., 19, 215-218, 1992.
793 Hansen, J., Ruedy, R., Glascoe, J., and Sato, M.: GISS analysis of surface temperature
794 change, J. Geophys. Res., 104, 30997-31022, 1999.
795 Hardy, D.R., Vuille, M., and Bradley, R.S.: Variability of snow accumulation and
796 isotopic composition on Nevado Sajama, Bolivia, J. Geophys. Res., 108, 4693, 2003.
797 Harshvardhan, and R.D. Cess: Stratospheric aerosols: effect upon atmospheric
798 temperature and global climate, Tellus, 28, 1-10, 1976.
799 Haywood, J.M., Jones, A., Bellouin, N., and Stephenson, D.: Asymmetric forcing from
800 stratospheric aerosols impacts Sahelian rainfall, Nature Climate Change, 3, 660-665,
801 2013.
802 Hegerl, G.C., Crowley, T.J., Baum, S.K., Kim, K.Y., and Hyde, W.T.: Detection of
803 volcanic, solar and greenhouse gas signals in paleo-reconstructions of Northern
804 Hemispheric temperature, Geophys. Res. Lett., 30, 1242, 2003.
805 Hegerl, G.C., Crowley, T.J., Hyde, W.T., and Frame, D.J.: Climate sensitivity

806 constrained by temperature reconstructions over the past seven centuries, Nature, 440,
807 1029–1032, 2006.
808 Held, I.M., and Soden, B.J.: Robust Responses of the Hydrological Cycle to Global
809 Warming, J. Climate, 19, 5686–5699, 2006.
810 Hoffmann, G., and Heimann, M.: Water isotope modeling in the Asian monsoon region,
811 Quat. Inter., 37, 115–128, 1997.
812 Iles, C.E., Hegerl, G.C., Schurer, A.P., and Zhang, X.: The effect of volcanic eruptions on
813 global precipitation, J. Geophys. Res. Atmos., 118, 8770–8786, 2013.
814 Iles, C. E., and Hegerl G. C., The global precipitation response to volcanic eruptions in
815 the CMIP5 models, Environ. Res. Lett., 9, 104012, 2014.
816 Joseph, R., and Zeng, N.: Seasonally Modulated Tropical Drought Induced by Volcanic
817 Aerosol, J. Climate, 24, 2045–2060, 2011.
818 Kang, S.M., Held I.M., Frierson, D.M.W., and Zhao, M.: The Response of the ITCZ to
819 Extratropical Thermal Forcing: Idealized Slab-Ocean Experiments with a GCM, J.
820 Climate, 21, 3521–3532, 2008.
821 Kang, S.M., Frierson, D.M.W., and Held, I.M.: The Tropical Response to Extratropical
822 Thermal Forcing in an Idealized GCM: The Importance of Radiative Feedbacks and
823 Convective Parameterization, J. Atmos. Sci., 66, 2812–2827, 2009.
824 Kang, S., Polvani, L., Fyfe, J., and Sigmond, M.: Impact of polar ozone depletion on
825 subtropical precipitation, Science, 332, 951–954, 2011.
826 Kang, S. M., Frierson, D. M., and Held, I. M.: The tropical response to extratropical
827 thermal forcing in an idealized GCM: The importance of radiative feedbacks and
828 convective parameterization, J. Atmos. Sci., 66, 2812–2827, 2009.

829 Kanner, L. C., Burns, S. J., Cheng, H., and Edwards, R. L.: High-latitude forcing of the
830 South American summer monsoon during the last glacial, Science, 335, 570–573,
831 2012.
832 Kanner, L. C., Burns, S. J., Cheng, H., Edwards, R. L., and Vuille, M.: High-resolution
833 variability of the South American summer monsoon over the last seven millennia:
834 insights from a speleothem record from the central Peruvian Andes, Quat. Sci. Rev.,
835 75, 1–10, 2013.
836 Kaplan, J. O., Krumhardt, K. M., Ellis, E. C., Ruddiman, W. F., Lemmen, C., and
837 Goldewijk, K. K.: Holocene carbon emissions as a result of anthropogenic land cover
838 change, The Holocene, 21, 775-791, doi:10.1177/0959683610386983, 2011.
839 Karpechko, A. Y., Gillett, N. P., Dall'Amico, M., and Gray, L. J.: Southern Hemisphere
840 atmospheric circulation response to the El Chichón and Pinatubo eruptions in coupled
841 climate models, Q.J.R. Meteorol. Soc., 136, 1813–1822, 2010.
842 Krivova, N., Balmaceda, L., and Solanki, S.: Reconstruction of solar total irradiance
843 since 1700 from the surface magnetic flux, Astron. Astrophys., 467, 335–346, 2007.
844 Lacis, A., Hansen, J., and Sato, M.: Climate forcing by stratospheric aerosols, Geophys.
845 Res. Lett.,, 19, 1607– 1610, 1992.
846 Ledru, M.-P., Jomelli, V., Samaniego, P., Vuille, M., Hidalgo, S., Herrera, M., and Ceron,
847 C.: The Medieval climate anomaly and the Little Ice Age in the eastern Ecuadorian
848 Andes, Clim. Past, 9, 307–321, 2013.
849 LeGrande, A.N., and Schmidt, G.A.: Ensemble, water-isotope enabled, coupled general
850 circulation modeling insights into the 8.2-kyr event, Paleoceanography, 23, PA3207,
851 2008.

852 LeGrande, A.N., and Schmidt, G.A.: Sources of Holocene variability of oxygen isotopes
853 in paleoclimate archives, Clim. Past, 5, 441-455, 2009.
854 Lewis, S.C., LeGrande A.N., Kelley, M., and Schmidt, G.A.: Modeling insights into
855 deuterium excess as an indicator of water vapor source conditions, J. Geophys. Res.
856 Atmos., 118, 2, 243-262, 2013.
857 Lewis, S.C., LeGrande, A.N., Schmidt, G.A., and Kelley, M.: Comparison of forced
858 ENSO-like hydrological expressions in simulations of the pre-industrial and mid-
859 Holocene, J. Geophys. Res. Atmos., 119, 12, 7064-7082, 2014.
860 Lewis, S.C., LeGrande, A.N., Kelley, M., and Schmidt, G.A.: Water vapour source
861 impacts on oxygen isotope variability in tropical precipitation during Heinrich events,
862 Clim. Past, 6, 325-343, 2010.
863 Liu, X. and Battisti, D.S.: The Influence of Orbital Forcing of Tropical Insolation on the
864 Climate and Isotopic Composition of Precipitation in South America, J. Climate, 28 ,
865 4841-4862, 2015.
866 Lucht, W., Prentice, I. C., Myneni, R. B., Sitch, S., Friedlingstein, P., Cramer, W.,
867 Bousquet, P., Buermann, W., and Smith, B.: Climatic control of the high-latitude
868 vegetation greening trend and Pinatubo effect, Science, 296, 1687–1689, 2002.
869 Ludlow, F., Stine, A. R., Leahy, P., Murphy, E., Mayewski, P. A., Taylor, D., Killen, J.,
870 Baillie, M. G., Hennessy, M., and Kiely, G.: Medieval Irish chronicles reveal
871 persistent volcanic forcing of severe winter cold events, 431–1649 CE,
872 Environmental Research Letters, 8, 024 035, 2013.

873 Man, W., Zhou, T., and Jungclaus, J. H.: Effects of large volcanic eruptions on global
874 summer climate and East Asian monsoon changes during the last millennium:
875 Analysis of MPI-ESM simulations, J. Climate, 27, 7394–7409, 2014.
876 Mann, M. E., Cane, M. A., Zebiak, S. E., and Clement, A.: Volcanic and solar forcing of
877 the tropical Pacific over the past 1000 years, J. Climate, 18, 447–456, 2005.
878 Marengo, J., Liebmann, B., Grimm, A., Misra, V., Silva Dias, P., Cavalcanti, I., Carvalho,
879 L., Berbery, E., Ambrizzi, T., Vera, C. S., Saulo, A. C., Nogues-Paegle, J., Zipser, E.,
880 Seth, A., and Alves, L. M.: Recent developments on the South American monsoon
881 system, Int. J. Climatol., 32, 1–21, 2012.
882 Marengo, J. A., Liebmann, B., Kousky, V. E., Filizola, N. P., and Wainer, I. C.: Onset
883 and end of the rainy season in the Brazilian Amazon Basin, J. Climate, 14, 833–852,
884 2001.
885 McGregor, H. V., M. N. Evans, H. Goosse, G. Leduc, B. Martrat, J. A. Addison, P. G.
886 Mortyn, D. W. Oppo, M.-S. Seidenkrantz, M.-A. Sicre, S. J. Phipps, K. Selveraj, K.
887 Thirumalai, H. L. Filipsson and V. Ersek: Robust global ocean cooling trend for the
888 pre-industrial Common Era, Nat. Geosci*,* 8, 671-677, 2015.
889 Miller, G. H., Geirsdóttir, Á., Zhong, Y., Larsen, D. J., Otto-Bliesner, B. L., Holland, M.
890 M., Bailey, D. A., Refsnider, K. A., Lehman, S. J., Southon, J. R., Anderson, C.,
891 Bjornsson, H., and Thordarson, T. Anderson, C., Bjornsson, H., and Thordarson, T..:
892 Abrupt onset of the Little Ice Age triggered by volcanism and sustained by sea-
893 ice/ocean feedbacks, Geophys. Res. Lett., 39, 2012.
894 Miller, R.L., Schmidt, G.A., Nazarenko, L.S., Tausnev, N., Bauer, S.E., Del Genio, A.D.,
895 Kelley, M., Lo, K.K., Ruedy, R., Shindell, D.T., Aleinov, I., Bauer, M., Bleck, R.,

Canuto, V., Chen, Y.-H., Cheng, Y., Clune, T.L., Faluvegi, G., Hansen, J.E., Healy, R.J., Kiang, N.Y., Koch, D., Lacis, A.A., LeGrande, A.N., Lerner, J., Menon, S., Oinas, V., Pérez García-Pando C., Perlwitz, J.P., Puma, M.J., Rind, D., Romanou, A., Russell, G.L., Sato, M., Sun, S., Tsigaridis, K., Unger, N., Voulgarakis, A., Yao, M.-S., and Zhang, J.: CMIP5 historical simulations (1850-2012) with GISS ModelE2, J. Adv. Model. Earth Syst., 6, 2, 441-477, 2014.

Minnis, P., Harrison, E., Stowe, L., Gibson, G., Denn, F., Doelling, D., and Smith, W.: Radiative climate forcing by the Mount Pinatubo eruption, Science, 259, 1411–1415, 1993.

Neukom, R. and Gergis, J.: Southern Hemisphere high-resolution palaeoclimate records of the last 2000 years, The Holocene, 22, 501–524, 2012.

Nogués-Paegle, J. and Mo, K. C.: Alternating wet and dry conditions over South America during summer, Monthly Weather Review, 125, 279–291, 1997.

Nogués-Paegle, J., Mechoso, C. R., Fu, R., Berbery, E. H., Chao, W. C., Chen, T.-C., Cook, K., Diaz, A. F., Enfield, D., Ferreira, R., Grimm A, Kousky V, Liebmann, B, Marengo, J, Mo, K, Neelin, JD, Paegle, J, Robertson, A, Seth, A, Vera ,C, Zhou, J .: Progress in Pan American CLIVAR research: understanding the South American monsoon, Meteorológica, 27, 1–30, 2002.

Novello, V. F., Cruz, F. W., Karmann, I., Burns, S. J., Stríkis, N. M., Vuille, M., Cheng, H., Lawrence Edwards, R., Santos, R. V., Frigo, E., and Barreto E.A.S.: Multidecadal climate variability in Brazil's Nordeste during the last 3000 years based on speleothem isotope records, Geophys. Res. Lett.,, 39, 2012.

Oman, L., Robock, A., Stenchikov, G., Schmidt, G. A., and Ruedy, R.: Climatic response to high-latitude volcanic eruptions, J. Geophys. Res. Atmos., 110, 2005.

Oman, L., Robock, A., Stenchikov, G. L., and Thordarson, T.: High-latitude eruptions cast shadow over the African monsoon and the flow of the Nile, Geophys. Res. Lett.,, 33, 2006.

Peng, Y., Shen, C., Wang, W.-C., and Xu, Y.: Response of summer precipitation over Eastern China to large volcanic eruptions, J. Climate, 23, 818–824, 2010.

Pollack, J. B., Toon, O. B., Sagan, C., Summers, A., Baldwin, B., and Van Camp, W.: Volcanic explosions and climatic change: A theoretical assessment, J. Geophys. Res., 81, 1071–1083, 1976.

Pollack, J. B., Toon, O. B., and Wiedman, D.: Radiative properties of the background stratospheric aerosols and implications for perturbed conditions, Geophys. Res. Lett.,, 8, 26–28, 1981.

Pongratz, J., Reick, C., Raddatz, T., and Claussen, M.: A global land cover reconstruction AD 800 to 1992: Technical description, Max Planck Institute for Meteorology Rep. on Earth System Science 51, 72 pp., 2008.

Robock, A.: Volcanic eruptions and climate, Reviews of Geophysics, 38, 191–219, 2000.

Robock, A.: Volcanoes: Role in climate, Encyclopedia of atmospheric sciences, 10, 2494–2500, 2003.

Robock, A. and Mao, J.: The volcanic signal in surface temperature observations, J. Climate, 8, 1086–1103, 1995.

939 Robock, A., Adams, T., Moore, M., Oman, L., and Stenchikov, G.: Southern Hemisphere
940 atmospheric circulation effects of the 1991 Mount Pinatubo eruption, Geophys. Res.
941 Lett.,, 34, 2007.
942 Russell, G. L., Miller, J. R., and Rind, D.: A coupled atmosphere-ocean model for
943 transient climate change studies, Atmosphere-ocean, 33, 683–730, 1995.
944 Santer, B.D., Bonfils C., Painter J.F., Zelinka, M.D., Mears, C., Solomon, S., Schmidt,
945 G.A., Fyfe, J.C., Cole, J.N.S., Nazarenko, L., Taylor, K.E., and Wentz, F.J.:
946 Volcanic contribution to decadal changes in tropospheric temperature, Nature
947 Geosci., 7, 3, 185-189, 2014.
948 Sato, M., Hansen, J. E., McCormick, M. P., and Pollack, J. B.: Stratospheric aerosol
949 optical depths, 1850–1990, J. Geophys. Res. Atmos., 98, 22 987–22 994, 1993.
950 Schmidt, G. A., LeGrande, A. N., and Hoffmann, G.: Water isotope expressions of
951 intrinsic and forced variability in a coupled ocean-atmosphere model, J. Geophys.
952 Res. Atmos., 112, 2007.
953 Schmidt, G. A., Jungclaus, J. H., Ammann, C. M., Bard, E., Braconnot, P., Crowley, T. J.,
954 Delaygue, G., Joos, F., Krivova, N. A., Muscheler, R., Otto-Bliesner, B. L.,
955 Pongratz, J., Shindell, D. T., Solanki, S. K., Steinhilber, F., and Vieira, L. E. A.:
956 Climate forcing reconstructions for use in PMIP simulations of the last millennium
957 (v1.0), Geosci. Model Dev., 4, 33–45, 2011.
958 Schmidt, G. A., Jungclaus, J. H., Ammann, C. M., Bard, E., Braconnot, P., Crowley, T.
959 J., Delaygue, G., Joos, F., Krivova, N.A., Muscheler, R., Otto-Bliesner, B. L.,
960 Pongratz, J., Shindell, D. T., Solanki, S. K., Steinhilber, F., and Vieira, L. E. A.:

961 Climate forcing reconstructions for use in PMIP simulations of the Last Millennium
962 (v1.1), Geosci. Model Dev., 5, 185–191, 2012.
963 Schmidt, G. A., Kelley, M., Nazarenko, L., Ruedy, R., Russell, G. L., Aleinov, I., Bauer,
964 M., Bauer, S., Bhat, M. K., Bleck, R., Canuto, V., Chen, Y., Cheng, Y., Clune, T.
965 L., DelGenio, A., de Fainchtein, R., Faluvegi, G., Hansen, J. E., Healy, R. J.,
966 Kiang, N. Y., Koch, D., Lacis, A. A., LeGrande, A. N., Lerner, J., Lo, K. K.,
967 Matthews, E. E., Menon, S., Miller, R. L., Oinas, V., Oloso, A., Perlwitz, J., Puma,
968 M. J., Putman, W. M., Rind, D., Romanou, A., Sato, M., Shindell, D. T., Sun, S.,
969 Syed, R., Tausnev, N., Tsigaridis, K., Unger, N., Voulgarakis, A., Yao, M.-S., and
970 Zhang, J.: Configuration and assessment of the GISS ModelE2 contributions to the
971 CMIP5 archive, J. Adv. Model. Earth Syst., 6, 141–184, 2014a.
972 Schmidt, G. A., Annan, J. D., Bartlein, P. J., Cook, B. I., Guilyardi, E., Hargreaves, J. C.,
973 Harrison, S. P., Kageyama, M., LeGrande, A. N., Konecky, B., Lovejoy, S., Mann,
974 M. E., Masson-Delmotte, V., Risi, C., Thompson, D., Timmermann, A., Tremblay,
975 L.-B., and Yiou, P.: Using palaeo-climate comparisons to constrain future
976 projections in CMIP5, Clim. Past, 10, 221–250, 2014b.
977 Schmidt, G.A., Shindell, D.T., and Tsigaridis, K.: Reconciling warming trends, Nat.
978 Geosci., 7, 158-160, 2014c.
979 Schneider, U., Becker, A., Finger, P., Meyer-Christoffer, A.,Rudolf, B., Ziese, M.: GPCC
980 Full Data Reanalysis Version 6.0 at 2.5 °: Monthly Land-Surface Precipitation from
981 Rain-Gauges built on GTS-based and Historic Data, doi:10.5676/
982 10.5676/DWD_GPCC/FD_M_V6_250, 2011.

983 Schurer, A. P., Tett, S. F., and Hegerl, G. C.: Small influence of solar variability on
984 climate over the past millennium, Nat. Geosci., 7, 104–108, 2014.
985 Seth, A., Rojas, M., and Rauscher, S. A.: CMIP3 projected changes in the annual cycle of
986 the South American Monsoon, Climatic Change, 98, 331–357, 2010.
987 Shindell, D. T., Schmidt, G. A., Mann, M. E., and Faluvegi, G.: Dynamic winter climate
988 response to large tropical volcanic eruptions since 1600, J. Geophys. Res. Atmos.,
989 109, 2004.
990 Steinhilber, F., Beer, J., and Fröhlich, C.: Total solar irradiance during the Holocene,
991 Geophys. Res. Lett.,, 36, 2009.
992 Stenchikov, G. L., Kirchner, I., Robock, A., Graf, H.-F., Antuna, J. C., Grainger, R.,
993 Lambert, A., and Thomason, L.: Radiative forcing from the 1991 Mount Pinatubo
994 volcanic eruption, J. Geophys. Res. Atmos., 103, 13 837–13 857, 1998.
995 Stothers, R. B. and Rampino, M. R.: Historic volcanism, European dry fogs, and
996 Greenland acid precipitation, 1500 BC to AD 1500, Science, 222, 411–413, 1983.
997 Thompson, L. G., Mosley-Thompson, E., Davis, M. E., Lin, P.-N., Henderson, K. A.,
998 Cole-Dai, J., Bolzan, J. F., and Liu, K.-B.: Late glacial stage and Holocene tropical
999 ice core records from Huascaran, Peru, Science, 269, 46–50, 1995.
1000 Thompson, L. G., Davis, M., Mosley-Thompson, E., Sowers, T. A., Henderson, K. A.,
1001 Zagorodnov, V. S., Lin, P. N., Mikhalenko, V. N., Campen, R. K., Bolzan, J. F.,
1002 Cole-Dai, J., and Francou, B.: A 25 000-year tropical climate history from
1003 Bolivian ice cores, Science, 282, 1858–1864, 1998.

1004 Thompson, L. G., Mosley-Thompson, E., Brecher, H., Davis, M., León, B., Les, D., Lin,
1005 P.-N., Mashiotta, T., and Mountain, K.: Abrupt tropical climate change: Past and
1006 present, Proc. Natl. Acad. Sci., 103, 10536–10543, 2006.
1007 Timmreck, C.: Modeling the climatic effects of large explosive volcanic eruptions, Wiley
1008 Interdisciplinary Reviews: Climate Change, 3, 545–564, 2012.
1009 Trenberth, K. E. and Dai, A.: Effects of Mount Pinatubo volcanic eruption on the
1010 hydrological cycle as an analog of geoengineering, Geophys. Res. Lett.,, 34, 2007.
1011 Turco, R., Whitten, R., and Toon, O.: Stratospheric aerosols: Observation and theory,
1012 Rev. Geophys., 20, 233– 279, 1982.
1013 Van Breukelen, M., Vonhof, H., Hellstrom, J., Wester, W., and Kroon, D.: Fossil
1014 dripwater in stalagmites reveals Holocene temperature and rainfall variation in
1015 Amazonia, Earth Planet. Sc. Lett., 275, 54–60, 2008.
1016 Vera, C., Higgins, W., Amador, J., Ambrizzi, T., Garreaud, R., Gochis, D., Gutzler, D.,
1017 Lettenmaier, D., Marengo, J., Mechoso, C. R., Nogues-Paegle, J., Silva Dias, P. L.,
1018 and Zhang, C.: Toward a unified view of the American monsoon systems, J.
1019 Climate, 19, 4977–5000, 2006.
1020 Vimeux, F., Gallaire, R., Bony, S., Hoffmann, G., and Chiang, J. C.: What are the climate
1021 controls on δD in precipitation in the Zongo Valley (Bolivia)? Implications for the
1022 Illimani ice core interpretation, Earth Planet. Sc. Lett., 240, 205–220, 2005.
1023 Vimeux, F., Ginot, P., Schwikowski, M., Vuille, M., Hoffmann, G., Thompson, L. G.,
1024 and Schotterer, U.: Climate variability during the last 1000 years inferred from
1025 Andean ice cores: A review of methodology and recent results, Palaeogeogr.,
1026 Palaeoclimatol., Palaeoecol., 281, 229–241, 2009.

1027 Vuille, M. and Werner, M.: Stable isotopes in precipitation recording South American
1028 summer monsoon and ENSO variability: observations and model results, Clim.
1029 Dynam., 25, 401–413, 2005.
1030 Vuille, M., Bradley, R. S., Werner, M., Healy, R., and Keimig, F.: Modeling δ18O in
1031 precipitation over the tropical Americas: 1. Interannual variability and climatic
1032 controls, J. Geophys. Res. Atmos., 108, 2003a.
1033 Vuille, M., Bradley, R.S., Healy, R., Werner, M., Hardy D. R., Thompson, L. G., Keimig,
1034 F.: Modeling $d^{18}O$ in precipitation over the tropical Americas: 2. Simulation of the
1035 stable isotope signal in Andean ice cores, J. Geophys. Res., 108, D6, 4175, 2003b.
1036 Vuille, M., Burns, S., Taylor, B., Cruz, F., Bird, B., Abbott, M., Kanner, L., Cheng, H.,
1037 and Novello, V.: A review of the South American monsoon history as recorded in
1038 stable isotopic proxies over the past two millennia, Clim. Past, 8, 1309–1321, 2012.
1039 Wilmes, S., Raible, C., and Stocker, T.: Climate variability of the mid-and high-latitudes
1040 of the Southern Hemisphere in ensemble simulations from 1500 to 2000 AD, Clim.
1041 Past, 8, 373–390, 2012.
1042 Yoshimori, M., Stocker, T. F., Raible, C. C., and Renold, M.: Externally forced and
1043 internal variability in ensemble climate simulations of the Maunder Minimum, J.
1044 Climate, 18, 4253–4270, 2005.
1045 Zhang, D., Blender, R., and Fraedrich, K.: Volcanoes and ENSO in millennium
1046 simulations: Global impacts and regional reconstructions in East Asia, Theor. Appl.
1047 Climatol., 111, 437–454, 2013.
1048 Zhou, J. and Lau, K.: Does a monsoon climate exist over South America? J. Climate, 11,
1049 1020–1040, 1998.

1050 Table 1: Time of Eruptions and Global Aerosol Optical Depth (AOD) from Crowley and

1051 Unterman (2013). List of eruptions used in study.

1052

Table 1. List of LM and L20 Eruptions

Start Date of Eruption[a]	Seasons in LM Composite		Max AOD[b]
	DJF[c]	JJA	
Jan 971	972	971-972	0.22
Jan 1193	1194	1193-1194	0.16
Jul 1228	1229-1251	1229-1230	0.38
Oct 1257	1258-1260	1258-1259	0.69
Jan 1286	1287-1288	1286-1287	0.28
Jul 1455	1456-1458	1456-1458	0.41
Jan 1600	1601	1600	0.17
Jan 1641	1642	1641-1642	0.24
May 1673	1674	1674	0.21
Apr 1694	1695-1697	1694-1696	0.24
Jan 1809	1810-1811	189-1810	0.30
May 1815	1816-1818	1815-1817	0.47
May 1835	1836	1835-1836	0.24
Jan 1883	1884	1884	0.20
Apr 1963[d]			0.11
Apr 1982[d]			0.12
Jun 1991	1992	1992	0.18

[a]Start of Eruption dates based on when they can be identified in the Crowley /Sato time-series averaged over the latitude band from 30°S to 30°N. May be slightly different than actual eruption date.

[b]Maximum AOD over the 30°S to 30°N latitude band encountered in monthly time-series during the duration of each event.

[c]December in year prior to listed date.

[d]Mt. Agung and El Chichón included in L20 but not LM composites.

1053

1054

1055

List of Figure Captions

Figure. 1. Aerosol Optical Depth (AOD) used to force the NASA GISS ModelE2-R over the Last Millennium and (bottom) zoomed in on the period 1950-1999 (Crowley+Sato) as discussed in text. AOD is the vertically integrated (15-35 km) and latitudinal average from 30°S to 30°N. Note difference in vertical scale between graphs. Orange dashed line marks the AOD threshold for defining a LM eruption in the present study. Eruption events defined in text must sustain the threshold AOD for at least one year, so not all events above the orange dashed line are used in the composites.

Figure. 2. (Top) Observed Climatological Precipitation for DJF (shading, in mm day^{-1}). SAMS box is drawn over the domain from 20°S to 0°, 77.5°W to 45°W and used for Figure 9 and 12. Data from the GPCP product, long-term climatological rainfall derived from years 1981 - 2010. (Bottom) As above, except for JJA. Box from 0° to 10°N, 77.5°W to 52.5°W used in averaging for Figures 9 and 12.

Figure. 3. Seasonal cycle (DJF minus JJA) of precipitation in **a)** GPCP precipitation product, from data in Figure 2 **b)** in ModelE2-R c) $\delta^{18}O_p$ in GNIP data d) and $\delta^{18}O_p$ in ModelE2-R. GNIP data only shown for stations with at least 90 reported $\delta^{18}O_p$ values at a given station from 1960-present, in addition to at least ten data values for each month: December, January, February, June, July, and August. Stations with seasonal differences of less than +/- 1.0 per mil are also omitted in panel (c).

Figure. 4. Composite tropical (30°S to 30°N) temperature response following the L20 volcanic eruptions. Fill colors denote observed monthly anomalies using GISTEMP, with 24-month running average shown as solid black line. ModelE2-R ensemble mean is shown as solid orange line and dashed grey lines indicate the six individual ensemble members. Anomalies are referenced to 5 years prior to eruptions (years -5 to 0). Dashed purple lines encompass the 5-95% interval for monthly tropical-mean temperature anomalies (relative to the previous five-year mean) in the GISTEMP product from 1950-present. The calculation of this range omits data two years after the L20 eruptions. The range is not symmetric about zero due to the tropical warming trend during this interval. All data are based on the ENSO-removal technique discussed in text.

Figure 5. Annual-mean temperature change (°C, ocean masked) for each L20 eruption (labeled on plot) in GISTEMP (top row) and each ModelE2-R ensemble member, as discussed in text. All plots use ENSO-removal procedure described in text.

Figure. 6. As in Figure 5, except for precipitation change (mm day^{-1}).

Figure. 7. Last Millennium post-volcanic temperature composite (°C) averaged over all 45 events during **a)** DJF and **b)** JJA from GISS ModelE2-R using procedure described in text. Stippling highlights areas with anomalies significant at $p<0.1$.

1100 **Figure. 8**. Last Millennium post-volcanic precipitation composite (mm day^{-1}) with all
1101 eruption events during **a)** DJF and **b)** JJA from GISS ModelE2-R using procedure
1102 described in text. Stippling highlights areas with anomalies significant at $p<0.1$.
1103
1104 **Figure. 9**. **a)** Average temperature anomaly during DJF within the SAMS region (red,
1105 20°S to 0°, 77.5°W to 45°W) and equatorial South America during JJA (blue, 0° to 10°N,
1106 77.5°W to 52.5°W) plotted against the peak AOD for all 15 eruptions (each point
1107 averaged over three ensemble members with the three member spread shown as
1108 horizontal bars) and **b)** As in a), but for precipitation. Dashed horizontal lines indicate the
1109 5-95% range for a two-season average of each variable relative to the previous 15 years
1110 (averaged over the same domain) in the entire control simulation with no external forcing.
1111 In both panels, the correlation coefficient and p-value are reported for a) temperature and
1112 b) precipitation vs. $\Delta\delta^{18}O_p$ in each season and over the same domain. The regression uses
1113 all 45 volcanic events.
1114
1115 **Figure. 10**. Last Millennium post-volcanic oxygen isotope in precipitation ($\Delta\delta^{18}O_p$)
1116 composite (per mil) with all eruption events during **a)** DJF and **b)** JJA from GISS
1117 ModelE2-R using procedure described in text. Stippling highlights areas with anomalies
1118 significant at $p<0.1$.
1119
1120 **Figure. 11**. Last Millennium Hovmöller diagram (10 years, time moving forward going
1121 upward, with year number labeled next to each month) for **a)** temperature anomaly (°C)
1122 **b)** precipitation anomaly (mm day^{-1}) using procedure described in text. Solid black lines

mark closest January to start of each eruption used in composite. **c)** Same as panel b, except zoomed in on 10 °S to 10 °N and over 3 years of time beginning with the January closest to each eruption. Red line in panel c shows latitude of maximum climatological precipitation as a function of time of year. All results zonally averaged in model from 77.5°W to 45°W. **d)** Last Millennium Hovmöller diagram for oxygen isotopes in precipitation (per mil).

Figure. 12. Frequency distribution of 100 random 45-event composites in LM control simulation of ModelE2-R (blue) for temperature (top row), precipitation (middle), and oxygen isotopes in precipitation (bottom) for DJF (left column) and JJA (right column). Results averaged over same domains as in Figure 9. Normal distribution with a mean and standard deviation equal to that of the data shown in red. Purple square shows the single 45-event composite used in this study, with the distribution of individual 15 volcanic eruptions (each averaged over three ensemble members) in black dots.

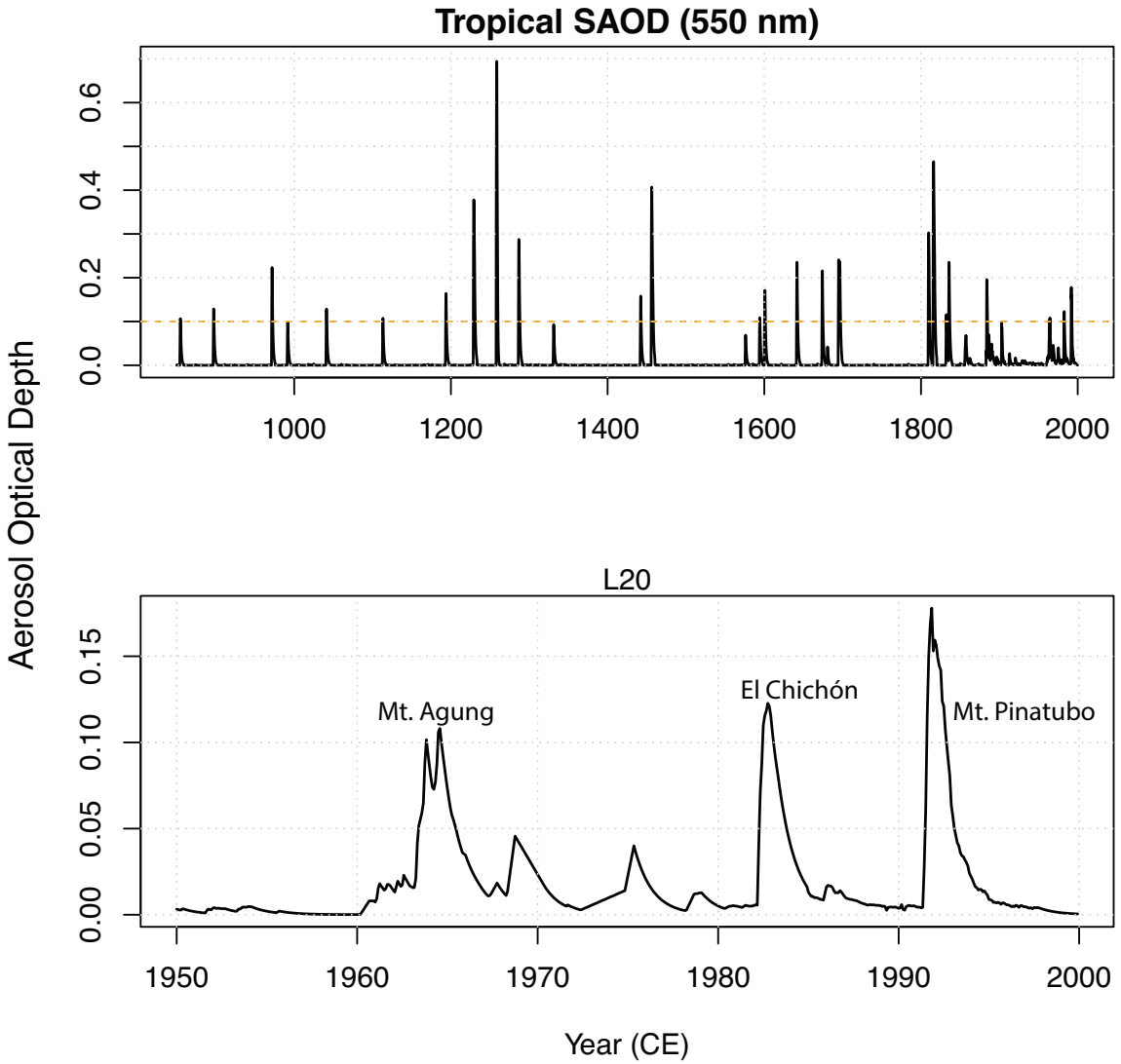

Figure. 1. Aerosol Optical Depth (AOD) used to force the NASA GISS ModelE2-R over the Last Millennium and (bottom) zoomed in on the period 1950-1999 (Crowley+Sato) as discussed in text. AOD is the vertically integrated (15-35 km) and latitudinal average from 30°S to 30°N. Note difference in vertical scale between graphs. Orange dashed line marks the AOD threshold for defining a LM eruption in the present study. Eruption events defined in text must sustain the threshold AOD for at least one year, so not all events above the orange dashed line are used in the composites.

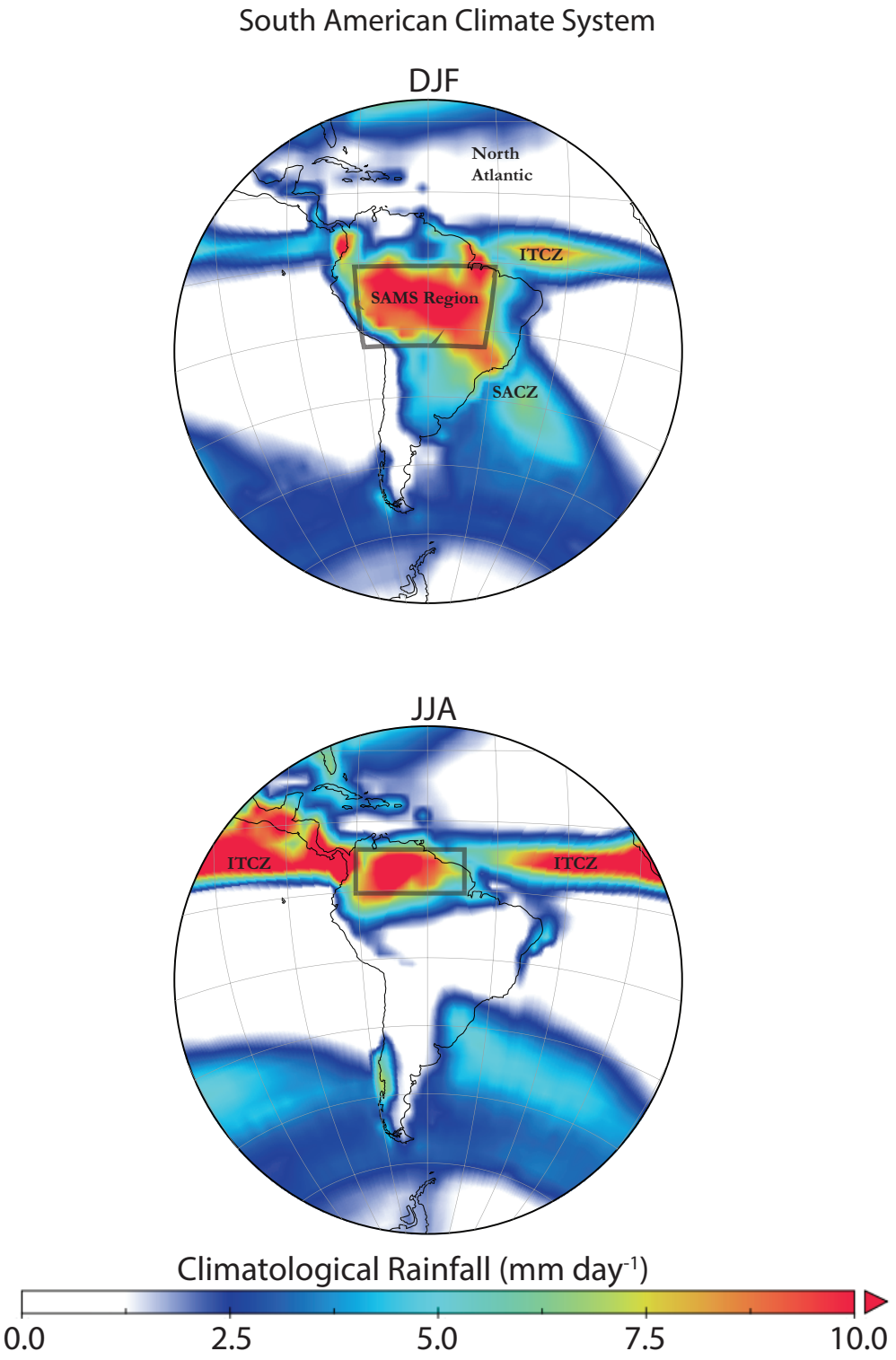

Figure. 2. (Top) Observed Climatological Precipitation for DJF (shading, in mm day^{-1}). SAMS box is drawn over the domain from 20°S to 0°, 77.5°W to 45°W and used for Figure 9 and 12. Data from the GPCP product, long-term climatological rainfall derived from years 1981 - 2010. (Bottom) As above, except for JJA. Box from 0° to 10°N, 77.5°W to 52.5°W used in averaging for Figures 9 and 12.

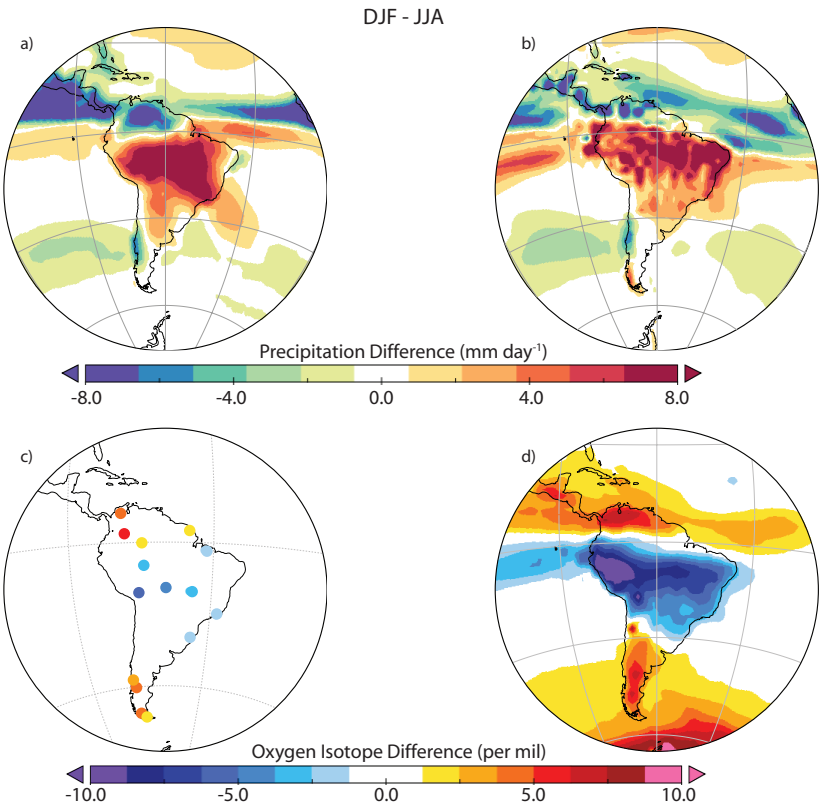

Figure. 3. Seasonal cycle (DJF minus JJA) of precipitation in **a)** GPCP precipitation product, from data in Figure 2 **b)** in ModelE2-R c) $\delta^{18}O_p$ in GNIP data d) and $\delta^{18}O_p$ in ModelE2-R. GNIP data only shown for stations with at least 90 reported $\delta^{18}O_p$ values at a given station from 1960-present, in addition to at least ten data values for each month: December, January, February, June, July, and August. Stations with seasonal differences of less than +/- 1.0 per mil are also omitted in panel (c).

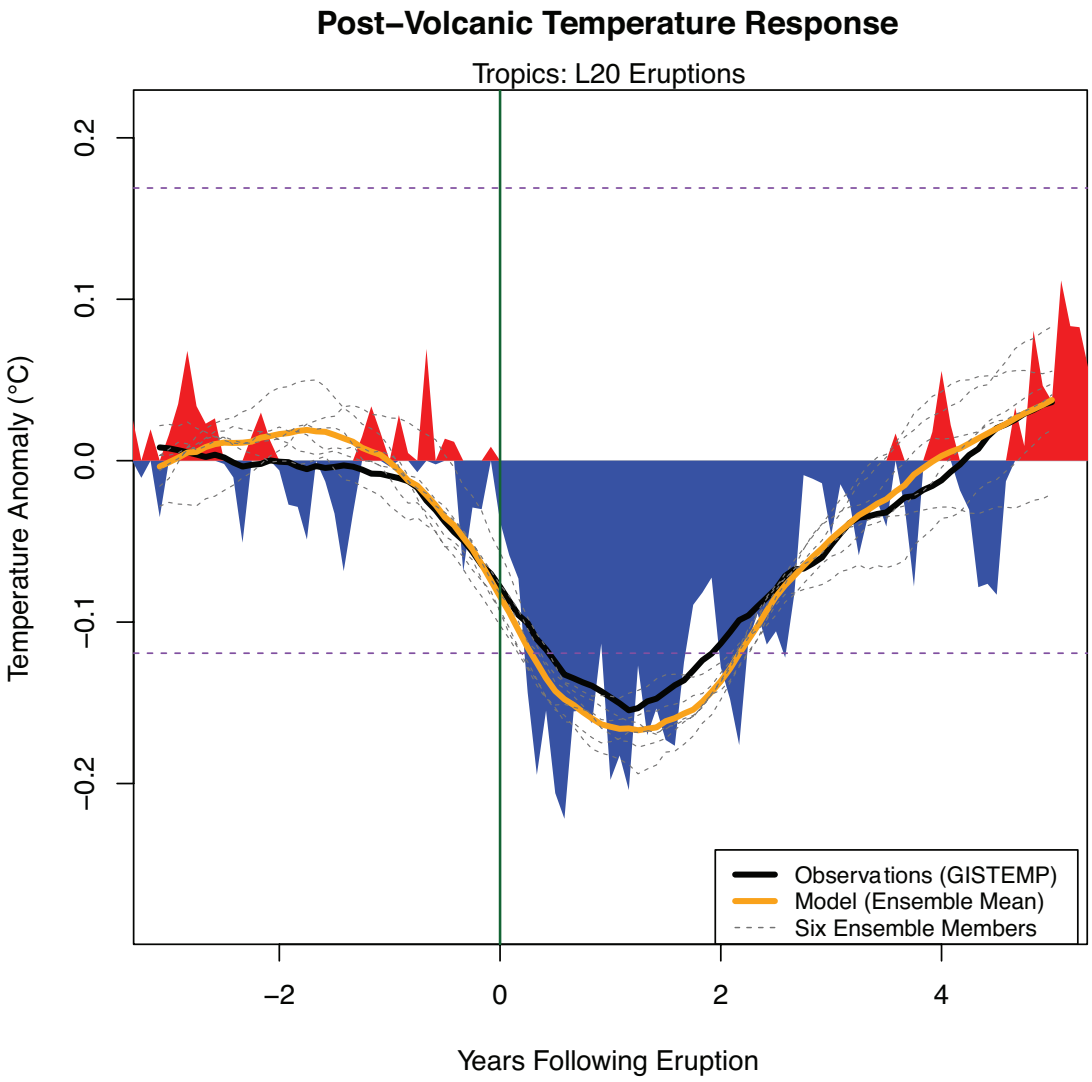

Figure. 4. Composite tropical (30°S to 30°N) temperature response following the L20 volcanic eruptions. Fill colors denote observed monthly anomalies using GISTEMP, with 24-month running average shown as solid black line. ModelE2-R ensemble mean is shown as solid orange line and dashed grey lines indicate the six individual ensemble members. Anomalies are referenced to 5 years prior to eruptions (years -5 to 0). Dashed purple lines encompass the 5-95% interval for monthly tropical-mean temperature anomalies (relative to the previous five-year mean) in the GISTEMP product from 1950-present. The calculation of this range omits data two years after the L20 eruptions. The range is not symmetric about zero due to the tropical warming trend during this interval. All data are based on the ENSO-removal technique discussed in text.

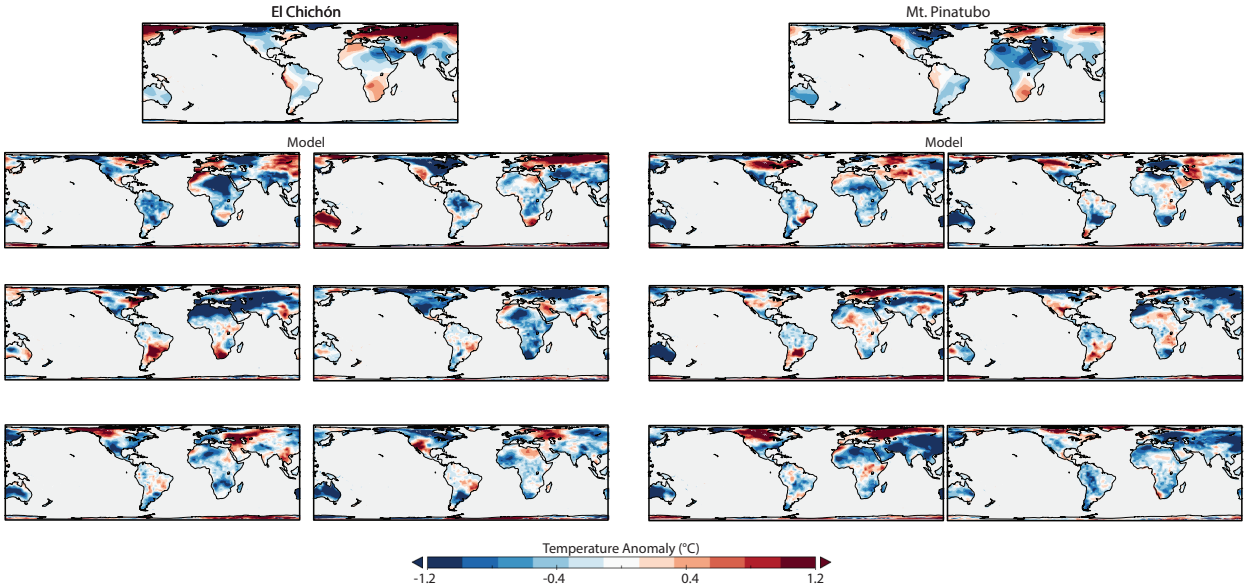

Figure 5. Annual-mean temperature change (°C, ocean masked) for each L20 eruption (labeled on plot) in GISTEMP (top row) and each ModelE2-R ensemble member, as discussed in text. All plots use ENSO-removal procedure described in text.

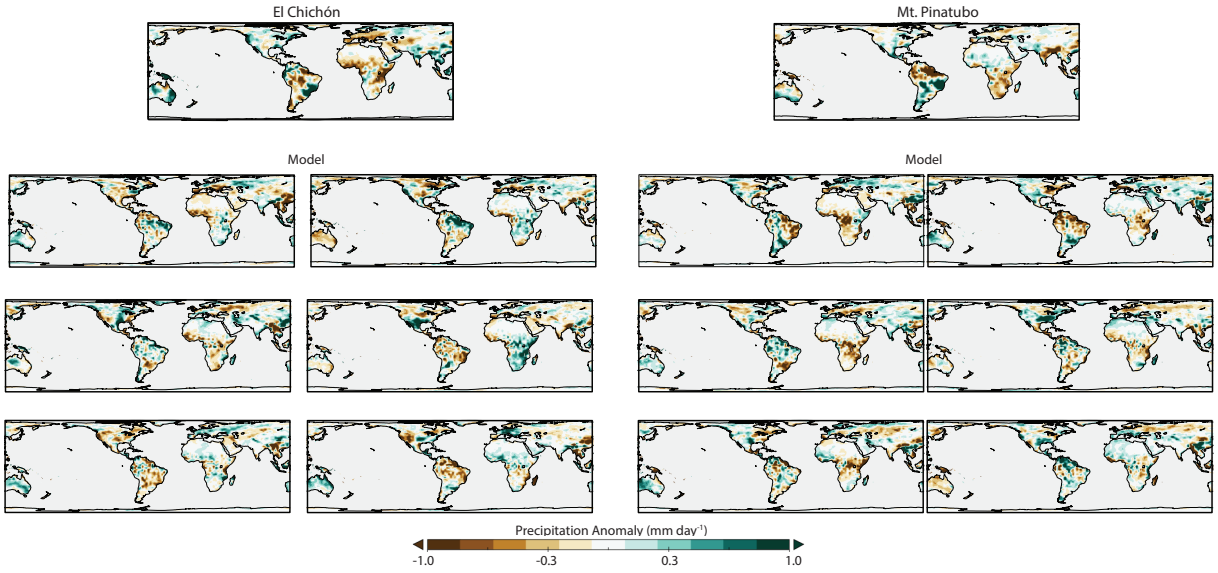

Figure. 6. As in Figure 5, except for precipitation change (mm day^{-1}).

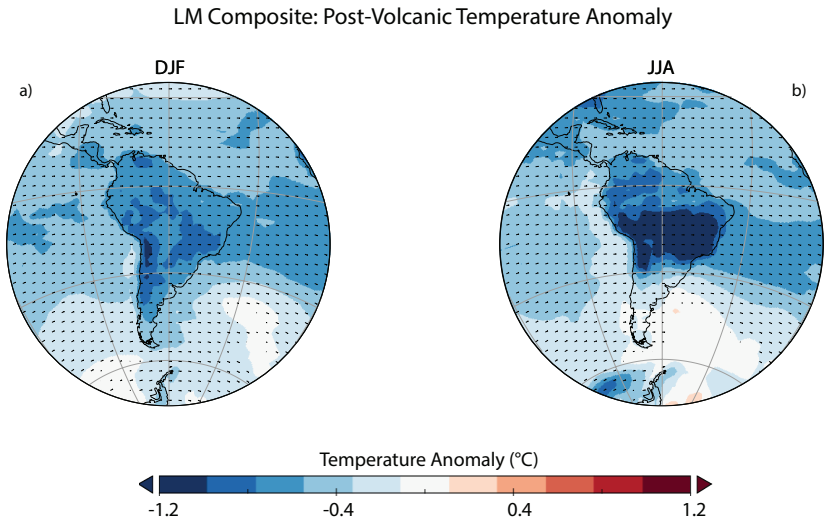

Figure. 7. Last Millennium post-volcanic temperature composite (°C) averaged over all 45 events during **a)** DJF and **b)** JJA from GISS ModelE2-R using procedure described in text. Stippling highlights areas with anomalies significant at $p<0.1$.

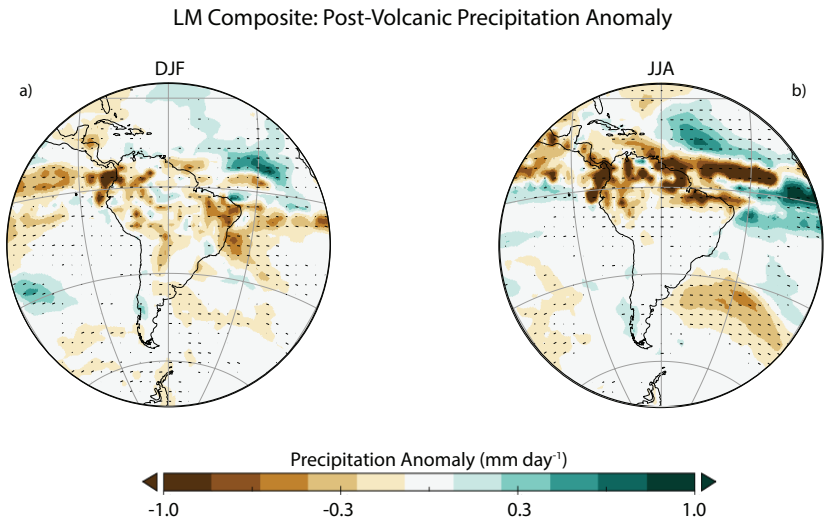

Figure. 8. Last Millennium post-volcanic precipitation composite (mm day^{-1}) with all eruption events during **a)** DJF and **b)** JJA from GISS ModelE2-R using procedure described in text. Stippling highlights areas with anomalies significant at $p<0.1$.

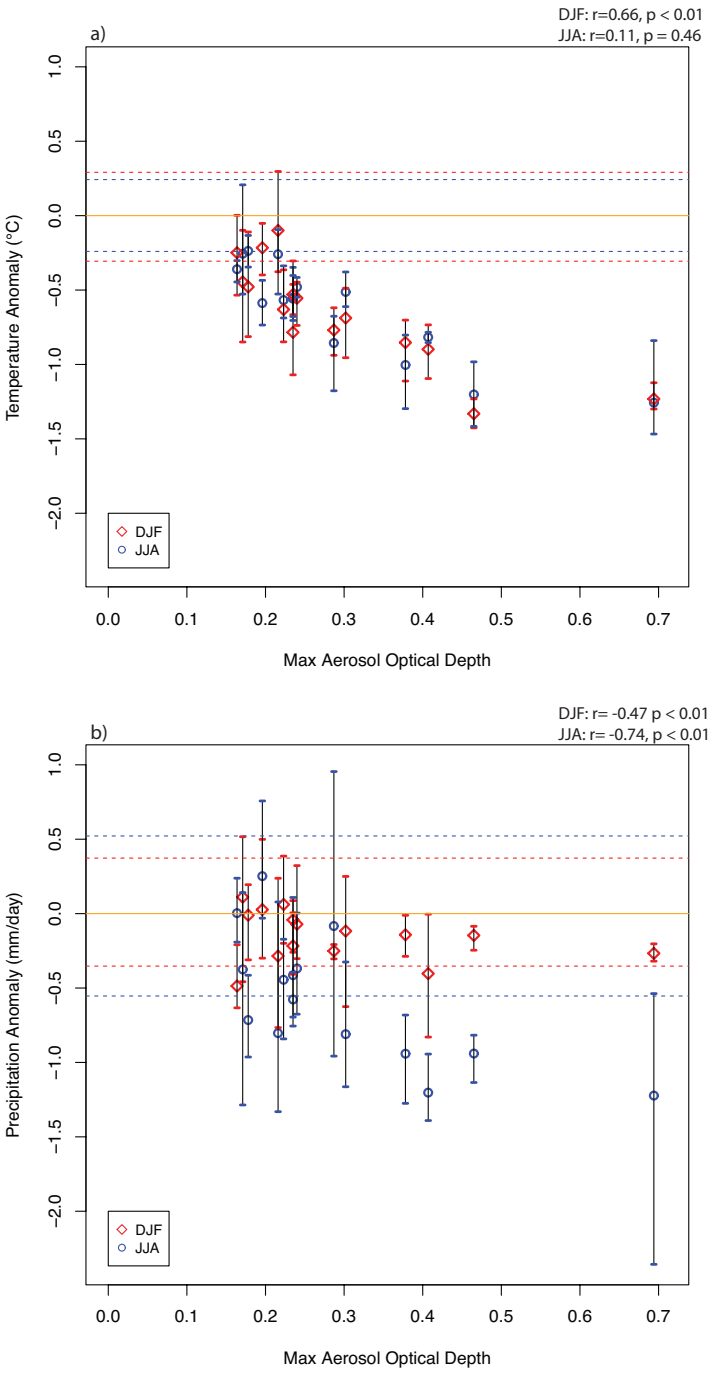

Figure. 9. **a)** Average temperature anomaly during DJF within the SAMS region (red, 20°S to 0°, 77.5°W to 45°W) and equatorial South America during JJA (blue, 0° to 10°N, 77.5°W to 52.5°W) plotted against the peak AOD for all 15 eruptions (each point averaged over three ensemble members with the three member spread shown as horizontal bars) and **b)** As in a), but for precipitation. Dashed horizontal lines indicate the 5-95% range for a two-season average of each variable relative to the previous 15 years (averaged over the same domain) in the entire control simulation with no external forcing. In both panels, the correlation coefficient and p-value are reported for a) temperature and b) precipitation vs. $\Delta\delta^{18}O_p$ in each season and over the same domain. The regression uses all 45 volcanic events.

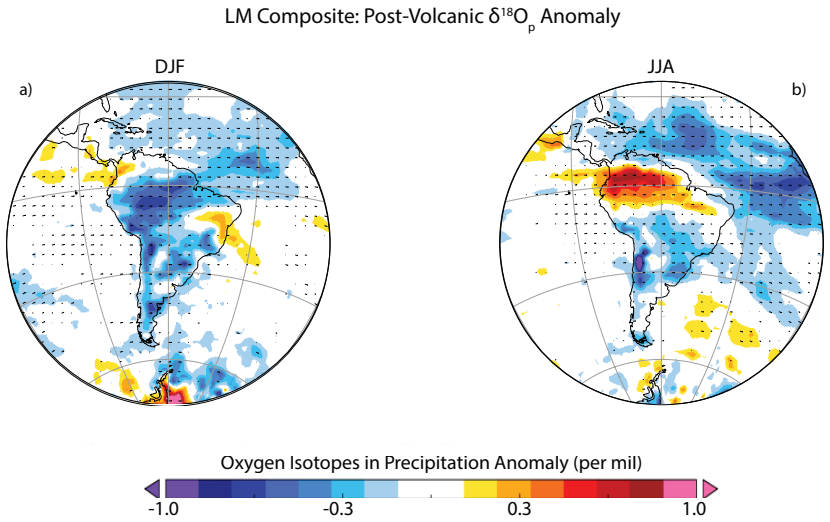

Figure. 10. Last Millennium post-volcanic oxygen isotope in precipitation ($\Delta\delta^{18}O_p$) composite (per mil) with all eruption events during **a)** DJF and **b)** JJA from GISS ModelE2-R using procedure described in text. Stippling highlights areas with anomalies significant at $p<0.1$.

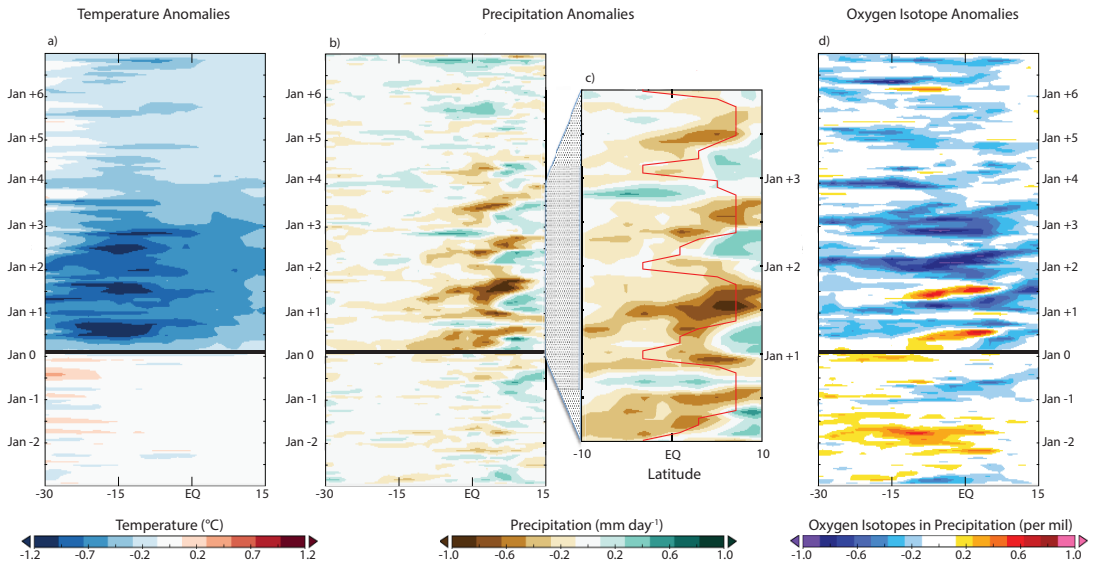

Figure. 11. Last Millennium Hovmöller diagram (10 years, time moving forward going upward, with year number labeled next to each month) for **a)** temperature anomaly (°C) **b)** precipitation anomaly (mm day^{-1}) using procedure described in text. Solid black lines mark closest January to start of each eruption used in composite. **c)** Same as panel b, except zoomed in on 10 °S to 10 °N and over 3 years of time beginning with the January closest to each eruption. Red line in panel c shows latitude of maximum climatological precipitation as a function of time of year. All results zonally averaged in model from 77.5°W to 45° W. **d)** Last Millennium Hovmöller diagram for oxygen isotopes in precipitation (per mil).

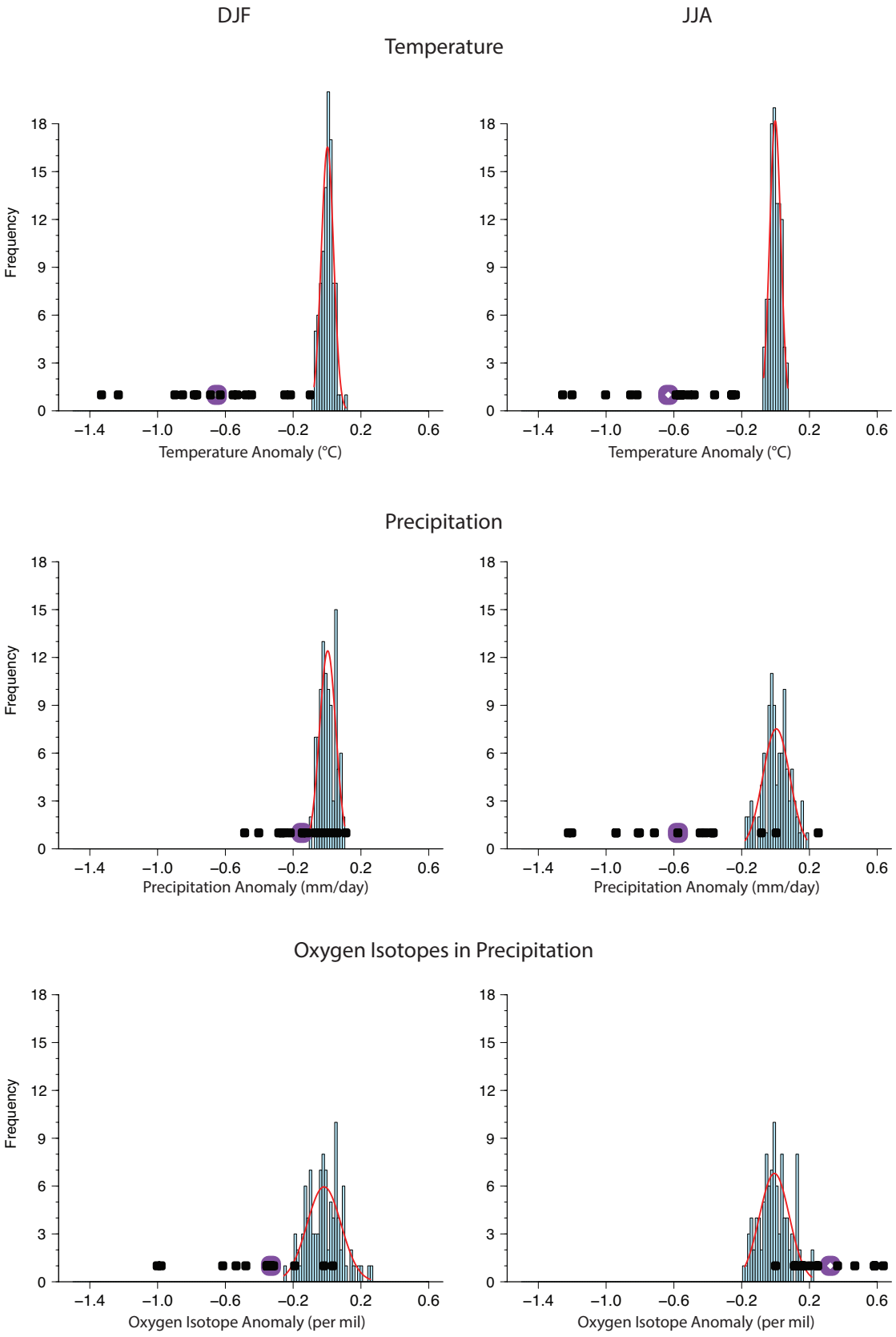
DJF
JJA
Temperature
Frequency
Temperature Anomaly (°C)
Precipitation
Precipitation Anomaly (mm/day)
Oxygen Isotopes in Precipitation
Oxygen Isotope Anomaly (per mil)

1285

Figure. 12. Frequency distribution of 100 random 45-event composites in LM control simulation of ModelE2-R (blue) for temperature (top row), precipitation (middle), and oxygen isotopes in precipitation (bottom) for DJF (left column) and JJA (right column). Results averaged over same domains as in Figure 9. Normal distribution with a mean and standard deviation equal to that of the data shown in red. Purple square shows the single 45-event composite used in this study, with the distribution of individual 15 volcanic eruptions (each averaged over three ensemble members) in black dots.